Materials Advances

ROYAL SOCIETY OF CHEMISTRY

PAPER

View Article Online
View Journal | View Issue

Cite this: *Mater. Adv.*, 2024, 5, 8111

Enhanced photocatalytic degradation and antimicrobial activities of biogenic Co_3O_4 nanoparticles mediated by fenugreek: sustainable strategies†

Arshdeep Kaur,[a] Sanjeev Kumar,*[b] Harpreet Kaur,[b] Gurmeet Singh Lotey,[c] Prit Pal Singh,[d] Gautam Singh,[l] Supreet,[e] Sunil Kumar,[f] Jasvir Dalal,*[g] Gassoumi Bouzid,[h] Mrinmoy Misra,[i] Raghvendra Pandey[j] and Sandeep Kaushal[k]

The present study introduces *Trigonella foenum-graecum* (TFG, fenugreek)-mediated Co_3O_4 nanoparticles (NPs) as an innovative solution for eliminating industrial azo dyes from contaminated water. The novelty lies in their rapid, cost-effective synthesis and excellent photocatalytic and antimicrobial performance, which mark a significant advancement in environmental remediation. The NPs are synthesized using a co-precipitation method and characterized through advanced techniques. UV-visible absorption spectroscopy revealed two prominent direct bandgap transitions, surpassing previous reports and enhancing light absorption for efficient photocatalysis. FTIR analysis confirmed the successful incorporation of TFG phytochemicals, while XRD and SAED patterns indicated high crystallinity, a small crystallite size (1.6 nm), and ultrafine average particle size (5.5 nm) as observed by HRTEM. XPS analysis validated the synthesis with controlled oxidation states and defect sites featuring Co^{2+} and Co^{3+} ions. The optimized synthesis process led to outstanding photocatalytic performance, achieving 100% degradation of Congo red dye in just 60 minutes at a concentration of 120 mg L^{-1}. This efficiency underscores their capability to treat CR-contaminated water under specific conditions. The synergy between TFG phytochemicals and Co_3O_4 NPs demonstrates significant potential for water pollution remediation. Additionally, these NPs exhibit strong antimicrobial activity against Gram-negative and Gram-positive bacteria, highlighting their broader environmental significance and potential applications in various ecological fields.

Received 6th August 2024,
Accepted 13th September 2024

DOI: 10.1039/d4ma00795f

rsc.li/materials-advances

1. Introduction

Green synthesis of nanoparticles, an advanced process with applications spanning energy, cosmetics, and more, offers distinct advantages over traditional methods mainly concerned with environmental sustainability and human health.[1–4] The traditional methods, including hydrothermal, sonochemical, sol–gel, and other techniques, involve the use of hazardous chemicals, high energy-inputs, and complex techniques that can have detrimental environmental impacts. These synthesis methods frequently employ toxic reagents and solvents resulting in the release of hazardous waste, more like the use of

[a] *Department of Physics, Sri Guru Granth Sahib World University, Fatehgarh Sahib – 140406, Punjab, India*
[b] *Department of Physics, Chandigarh University, Gharuan Mohali – 140413, India. E-mail: mann.khant91@gmail.com, kumarsanju25@gmail.com*
[c] *Department of Physics, IUPUI 402 N. Blackford St., LD 156U Indianapolis, IN 46202, USA*
[d] *Department of Chemistry, Sri Guru Granth Sahib World University, Fatehgarh Sahib – 140406, Punjab, India*
[e] *Amity School of Applied Sciences, Amity University, Haryana – 122412, India*
[f] *Department of Nanotechnology and Advanced Materials Engineering and HMC, Sejong University, Seoul 05006, South Korea*
[g] *Department of Physics, Rajdhani College, University of Delhi, Delhi – 110015, India. E-mail: jasvirdalal2012@gmail.com*
[h] *Laboratory of Advanced Materials and Interfaces (LIMA), University of Monastir, Faculty of Science of Monastir, Avenue of Environment, 5000, Monastir, Tunisia*
[i] *Mechatronics Engineering Department, School of Auto mobile, Mechanical and Mechatronics, Manipal University, 302034 Jaipur, India*
[j] *Department of Physics, ARSD College, University of Delhi, Delhi – 110021, India*
[k] *Regional Institute of Education, NCERT, Ajmer, Rajasthan – 305004, India*
[l] *Department of Applied Physics, Amity Institute of Applied Science, Amity University Uttar Pradesh, Noida, 201313, India*

† Electronic supplementary information (ESI) available. See DOI: https://doi.org/10.1039/d4ma00795f

hydrofluoric acid, reducing agents such as hydrazine or sodium borohydride, and capping/stabilizer agents like polyvinyl alcohol, which can lead to the formation of by-products that are difficult to manage and dispose of.[5] Furthermore, techniques like the hydrothermal method, Chemical vapor deposition technique, Physical vapor deposition, *etc.* often require high temperatures and pressures, which increase energy consumption.[5,6] In contrast, the green synthesis of nanoparticles offers a more environment-friendly alternative by utilizing natural resources and minimizing the use of toxic substances.[7] For green synthesis, plants that are rich in biomolecules such as flavonoids, terpenoids, and alkaloids, serve as valuable resources.[8–10] These biomolecules effectively combine with metal ions to facilitate nanoparticle production, with flavonoids playing a crucial role in ion reduction.[11] Derived from plants, these biomolecules are vital for capping nanomaterials, providing stability and biocompatibility, and participating in bio-reduction processes.[12,13] Thus, this method aligns with the principle of green chemistry, which emphasizes the reduction of hazardous (into eco-friendly products) and capping agents, energy efficiency, and the use of renewable sources, thereby controlling the environmental impact associated with the traditional synthesis methods.[7] Amid global concerns about antibiotic resistance, driven by overuse and environmental factors, there is an urgent need for novel approaches.[14–16] Nanoparticles, with their potential to enhance antibiotic effectiveness and mitigate resistance, offer promising solutions, especially in medical devices and implants.[17]

Various metals, including zinc (Zn),[15] copper (Cu),[16] silver (Ag),[17] iron (Fe),[18] titanium (Ti),[19] and gold (Au)[20] have been widely explored for plant-mediated NP synthesis from different plant species for photocatalytic degradation. However, their higher toxicity limits their use in medical applications.[21] Cobalt oxide nanoparticles (Co_3O_4 NPs), with spinel structure, antiferromagnetic properties, and p-type semiconductor characteristics, are gaining attention.[22] Co_3O_4 NPs have diverse applications in electrochemical devices, solar cells, energy storage, gas sensors, catalysis, and biomedicine. Also, Co_3O_4 NPs exhibit antibacterial, anticancer, antioxidant, antifungal, and enzyme-inhibitory properties, making them ideal for biomedical applications.[23] In addition, Co_3O_4 NPs serve as effective photocatalysts for dye degradation and environmental remediation, offering cost-effective alternatives to noble metals.[24] The green synthesis of Co_3O_4 NPs using plant extracts is considered a safe, inexpensive, and environmentally friendly method, resulting in stable materials. Various plants, such as *Calotropis procera*, *Sageretia thea*, *Moringa oleifera, etc.* have been explored for the green synthesis of Co_3O_4 NPs.[25–29] For instance, Diallo *et al.*,[30] utilized *Aspalathus linearis* leaf extract, while Dubey *et al.*,[26] employed *Calotropis procera latex* for cobalt oxide NP production. Bibi *et al.*[31] synthesized cobalt oxide NPs using *Punica granatum* peel extract.

Even with these advances, the biosynthesis of Co_3O_4 NPs utilizing *Trigonella foenum-graecum* (TFG, fenugreek) seed extract as a reducing and stabilizing agent remains unexplored. This study introduces a straightforward method for the green synthesis of Co_3O_4 NPs using TFG seed extract. *Trigonella foenum-graecum*, commonly known as methi or fenugreek, belongs to the Fabaceae family and holds significant value in traditional medicine.[32] It is widely cultivated in countries such as India, Egypt, France, Iran, Nepal, *etc*.[33,34] TFG seeds, known for treating various conditions, contain saponins with digestive enzyme inhibition properties and exhibit pharmacological qualities such as antilipidemic, anthelmintic, anti-inflammatory, and neuroprotective effects.[35,36] TFG seed extract, rich in triterpenoids, flavonoids, steroids, cardenolides, alkaloids, and other compounds, serves as a dual-functional agent, acting as both a reducing and capping agent during nanoparticles synthesis. This helps regulate NP shape, minimize aggregation, and stabilize the NPs.[37] Therefore, TFG-leaf extract has been utilized in the synthesis of various metal and metal oxide NPs (such as Ag, ZnO, and TiO_2) for applications in antimicrobial activity and dye degradation.[38–42] Specifically, for metal NPs, studies by Rizwana *et al.*, and Moond *et al.*, have demonstrated that silver (Ag) nanoparticles synthesized using TFG leaf extract were effective in inhibiting the growth of both Gram-positive and Gram-negative bacteria and in degrading different dyes, including Methylene Blue, Methyl Orange, and Rhodamine B.[39,40] Regarding metal oxides, Kermani *et al.*, evaluated the dye degradation capabilities of ZnO nanoparticles synthesized using TFG leaf extract, demonstrating significant degradation of Methylene Blue (MB) and Eriochrome Black T (EBT) under UV light.[41] Subhapriya *et al.*, synthesized spherical TiO_2 nanoparticles (20–90 nm) using TFG leaf extract, which exhibited excellent antimicrobial properties.[42] These above-mentioned findings highlight the potential of TFG extract (leaf extracts rather than seeds) mediated nanoparticles for photocatalytic degradation and antimicrobial applications. Thus, the present study aims to fill this gap by exploring the potential of TFG-seed extract as a novel, sustainable resource that can serve as an effective reducing and capping agent for the green synthesis of Co_3O_4.

To the best of our knowledge, this study is the first to report the use of TFG-seed extract for the synthesis of Co_3O_4 NPs for photocatalytic degradation and antimicrobial activities. In this study, these hypotheses are tested through a comprehensive analysis of the structural, morphological, and surface properties of the synthesized Co_3O_4 nanoparticles, demonstrating their exceptional photocatalytic degradation of Congo Red dye at two different catalyst doses and antimicrobial effectiveness against both Gram-positive *Staphylococcus aureus* and Gram-negative *Pseudomonas aeruginosa*. The successful synthesis of nanoparticles and findings reveals a sustainable strategy for nanoparticle production, demonstrating a commonly available and economically viable plant resource. This technique not only reduces reliance on toxic chemicals but also addresses pressing challenges such as water pollution and antibiotic resistance. Therefore, the present work underscores the novelty and potential for utilizing plant-based resources (using TFG seed extract) in developing advanced materials (Co_3O_4 NPs), promoting sustainable practices.

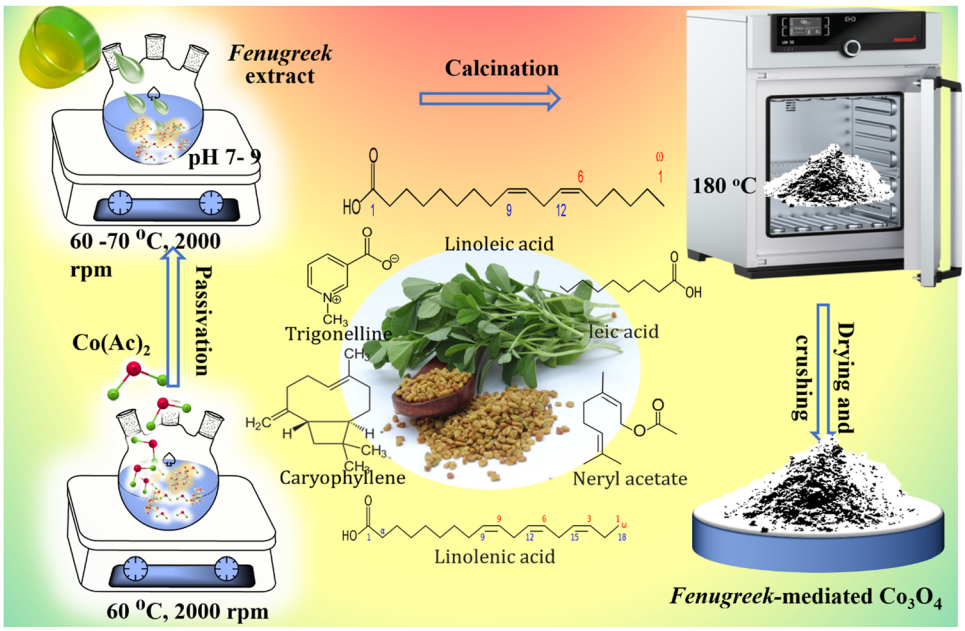

Fig. 1 Synthesis of *Trigonella foenum-graecum*-mediated Co_3O_4 nanoparticles.

2. Experimental details

The details of chemicals/materials used in the whole experiment, including the procedure of synthesis of the nanoparticles, and photocatalysis and antimicrobial activity are given in the supplementary file. A systematic synthesis process of *Trigonella foenum-graecum*-mediated Co_3O_4 nanoparticles is depicted in Fig. 1.

2.1. Formation mechanism of Co_3O_4 using TGF seed extract

The formation mechanism of Co_3O_4 nanoparticles using TFG seed extract begins with the preparation of an aqueous cobalt nitrate ($Co(NO_3)_2$) solution, where 0.1 M $Co(NO_3)_2{\cdot}6H_2O$ is dissolved in distilled water and stirred for 30 minutes. This ensures the complete dissolution of cobalt ions, providing a sufficient concentration of precursor ions for nanoparticle synthesis. Then, the seed extract comprised of phytochemicals, is added to the cobalt solution and heated (60–70 °C). The phytochemicals in the seed extract, such as alcohols, carboxylic acids, and ethers (FTIR), act as both reducing and capping agents.[1,43] Thus, the phytochemicals acting as reducing agents, start the reduction of Co^{2+} ions to Co^0, initiating the nucleation of Co_3O_4 nanoparticles, and temperature accelerates the reaction. Then pink to dark brown color change of the mixture indicates the successful reduction of cobalt ions and the formation of nanoparticles. After that, the interaction between cobalt particles and the phytochemicals takes place and it has a key role in influencing the shape of formed particles.[7,43] As the reaction proceeds, the phytochemicals acting as capping or stabilizing agents, adsorb onto the Co_3O_4 nanoparticle surface and influence the growth and stabilization of the particles. Due to uniform growth rates in all directions, facilitated by evenly distributed capping agents on the Co_3O_4 nanoparticle surface, the spherical shape is formed (FESEM). In contrast, non-spherical shapes emerge when the capping agents bind selectively to certain crystal facets, leading to anisotropic growth. As the Co_3O_4 nanoparticles continue to grow, their aggregation is minimized due to the presence of capping agents that prevent excessive particle–particle interactions. So, depending upon the excess or less availability of phytochemicals acting as stabilizing agents, an aggregation phenomenon occurs. This controlled aggregation leads to the development of distinct shapes both spherical and non-spherical due to the selective adsorption of different phytochemicals on various facets of the Co_3O_4 nanoparticles. These shapes are confirmed by FESEM and TEM analysis, which shows a mixture of semi-spherical and irregularly shaped particles. At last, the resulting Co_3O_4 nanoparticles were washed with distilled water and ethanol to remove any residual plant extract and impurities, ensuring their purity. And, the drying process at 100 °C for 4 hours eliminates moisture, and subsequent calcination at 180 °C for 2 hours enhances the crystallinity and stability of the Co_3O_4 nanoparticles.[43] The whole probable formation mechanism is as follows:

$$Co(NO_3)_2{\cdot}6H_2O \rightarrow Co^{2+} + 2NO^{3-} + 6H_2O \quad (1)$$

$$Co^{2+} + \text{TFG-Phytochemicals (reduced form)} \rightarrow Co^0/\text{TFG} + \text{TFG-Phytochemicals (oxidized form)} \quad (2)$$

$$Co/\text{TFG} + H_2O \rightarrow Co(OH)_2 + \text{2H-TFG compound} \quad (3)$$

$$6Co(OH)_2 + \text{2H-TFG compound} + \text{Heat} \rightarrow 2Co_3O_4 + 6H_2O + \text{2H-TFG compound} \quad (4)$$

Co_3O_4 + TFG-Phytochemicals → TFG-Capped Co_3O_4 nanoparticles → Crushing → washing → calcination (180 °C) → Crystalline-TFG-Capped Co_3O_4 nanoparticle (5)

3. Results and discussion

3.1. X-ray diffraction analysis

The crystallinity of nanoparticles was examined through X-ray diffraction (XRD) spectroscopy. Fig. 2 depicts the XRD spectra of Co_3O_4 NPs that were made from an ethanolic extract of TFG seeds. In Fig. 2a, the (220), (311), (222), (400), (422), (511), (440), and (531) planes of the Co_3O_4 NPs should be represented by distinct peaks at 2θ values of 31.61°, 37.21°, 39.23°, 45.28°, 56.11°, 59.73°, 65.61°, and 68.42° respectively. The results from the literature (JCPDS card No. 01-074-1657 (Fig. 2b)) are in good agreement with all the reflections in Fig. 2a and can be easily indexed to a face-centered phase of Co_3O_4. The absence of distinctive peaks of impurity phases like CoO and CoOOH shows the purity of the final products. The synthesized Co_3O_4 crystallites were confirmed to be pristine and devoid of any crystallographic anomalies by X-ray patterns of the particles, which showed sharp as well as narrow width peaks and agreed with previous reports in the literature.[44–46]

The average crystalline size of the cobalt oxide nanoparticles was calculated from the width of the XRD peaks, using the Debye–Scherrer method (eqn (6)).[47]

$$D = k\lambda/\beta\cos\theta \quad (6)$$

where, D = the size of the particle, k = Scherrer's constant, β = full width at half maxima of peaks in XRD, θ = corresponding angle for peaks, and λ = the X-ray wavelength. Table 1 shows the crystallographic parameters (*i.e.*, FWHM, *d*-spacing, and crystallite size of the peaks), and Bragg's law (eqn (7)) was used to find the inter-planner spacing between the atoms for every diffraction peak.[48]

$$2d\sin\theta = n\lambda \quad (7)$$

Table 1 Crystallographic parameters of TFG-mediated Co_3O_4 NPs

S. no.	2 Theta (degree)	Theta (radians)	FWHM β (degree)	FWHM β (radians)	*d*-Spacing	Crystallite size (*D*) (nm)
1	31.6194	0.275931319	8.20829	0.14326	2.82738	1.05
2	37.2124	0.324739451	5.11700	0.08931	2.41427	1.71
3	39.2354	0.342393457	3.41700	0.05964	2.29432	2.58
4	45.2874	0.39520712	11.88300	0.20740	2.00078	0.76
5	56.1164	0.489707972	4.72600	0.08248	1.63765	1.99
6	59.7374	0.521307158	4.62400	0.08070	1.54674	2.07
7	65.6194	0.572637292	4.19900	0.07329	1.42161	2.35
8	68.4244	0.597115534	12.71600	0.22194	1.37001	0.79

Average crystallite size = 1.6.

where n = integer, θ = Bragg's angle, d represents the inter-planar spacing and λ is the X-ray wavelength. FWHM was determined for each observed peak utilizing a Lorentz best-fit curve ($R^2 > 0.99$).

From the most intense peak (311), the crystallite size was calculated to be 1.71 nm, which was closely related to the average crystallite size (1.6 nm). In a previous report, a diameter (d) value of 26 nm was documented for Co_3O_4 NPs synthesized using *Curcuma longa* plant extract after drying at 100 °C for 60 min.[49] Another investigation reported a d value of 29.10 nm for Co_3O_4 NPs synthesized using *Piper nigrum* leaves extract with heating at 60 °C for 30 minutes and calcined at 600 °C and also reported a d value of 42.05 nm after calcined at 900 °C.[50] For low crystallinity, Co_3O_4 NPs made by aqueous leaf extract of *Mollugo oppositifolia* L. and calcined at 500 °C for 3 h, the crystallite size was reported 22.70 nm.[51] Consequently, it was inferred that the biomolecules present in the TFG seed extract function both as reducing and stabilizing agents, contributing to the synthesis of Co_3O_4 NPs with smaller crystallite sizes. This, in turn, will enhance the activation of the Co_3O_4 surface, promoting improved dye adsorption and photocatalytic activity.

Considering the above, the X-ray diffraction (XRD) investigation of the TFG-mediated Co_3O_4 NPs revealed detailed insights into their structural properties. As a result, the XRD analysis not only verified the effective synthesis of Co_3O_4 NPs utilizing

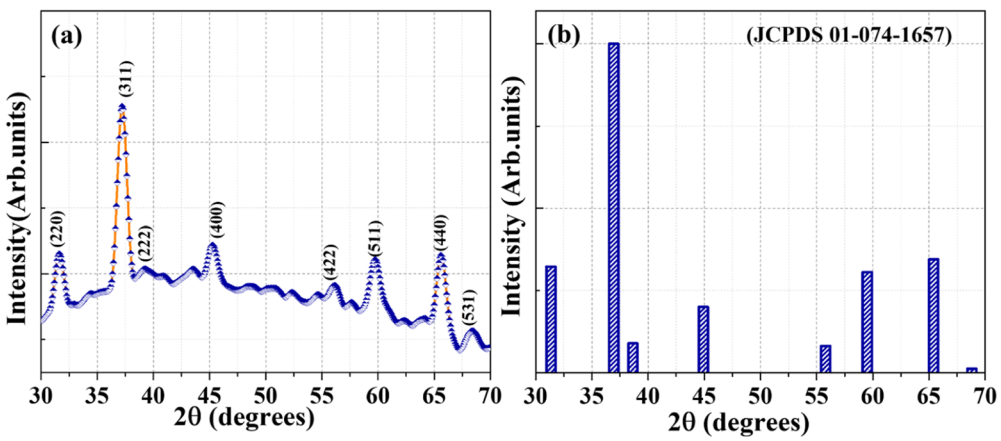

Fig. 2 (a) XRD pattern of TFG mediated Co_3O_4 NPs and (b) standard JCPDS of Co_3O_4.

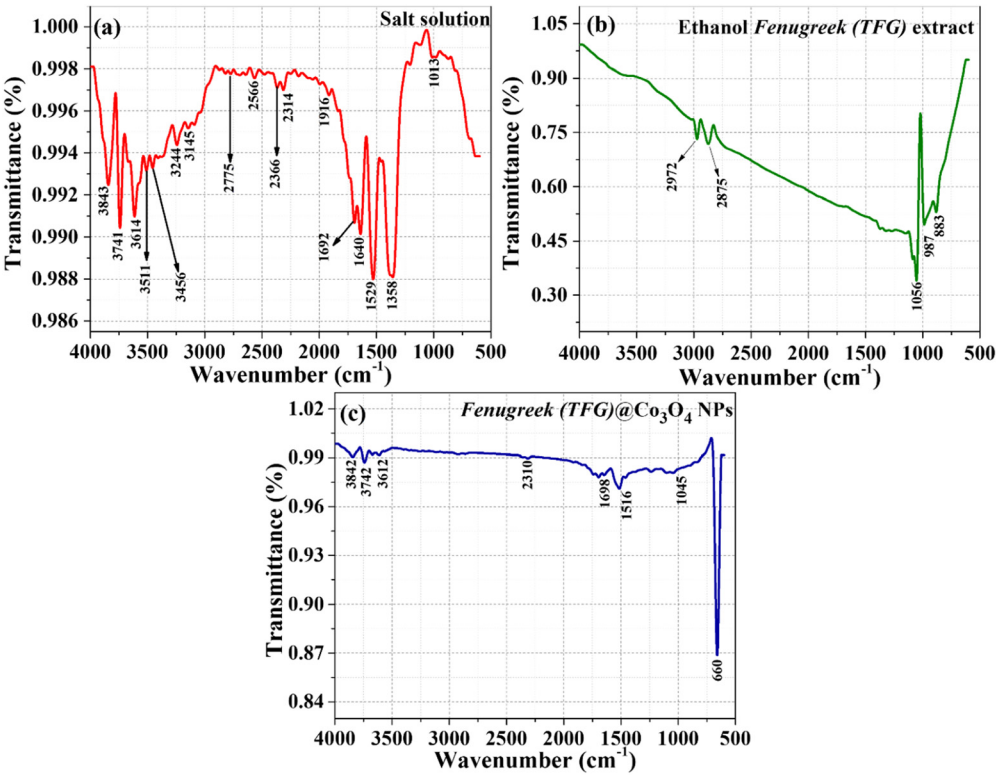

Fig. 3 FTIR analysis of (a) aqueous solution of the cobalt salt, (b) ethanol TFG seeds extract, and (c) TFG/Co_3O_4 NPs.

TFG-mediated techniques, but it also revealed critical information regarding their crystalline nature, purity, and size.

3.2. FTIR spectroscopic analysis

FTIR spectroscopy is often used to assess the structure and purity of metal or metal oxide nanoparticles (NPs). Each peak in the FTIR spectrum represents a particular vibrational mode of a chemical bond inside a molecule. These frequencies have been used to find functional groups or types of chemical bonds present in a sample. FTIR spectra of cobalt nitrate hexahydrate ($Co(NO_3)_2{\cdot}6H_2O$) salt solutions were measured between 500 and 4000 cm^{-1} (Fig. 3a). The peaks in the range of 3200–3600 cm^{-1} were corresponding to the O–H stretching vibration, which suggests the presence of water molecules in the hexahydrate. The carbonyl group (C═O), which is found in aldehydes, ketones, and carboxylic acids, was associated with the band at 2366 cm^{-1}. Furthermore, C═O ester, C═O carbonyl group, C═C bond in an aromatic ring, C–H bending vibrations in alkanes, and C–H bending vibrations in aromatic compounds were assigned to the bands at 1692, 1640, 1529, 1358, and 1013 cm^{-1}, respectively.[49,52]

Fig. 3b represents the FTIR spectrum of an ethanolic extract of TFG seeds in the 500–4000 cm^{-1} range. The symmetric and asymmetric C–H stretching vibrations in alkanes correlated with the peaks at 2972 and 2875 cm^{-1}, respectively. Where the peaks at 1056 and 987 cm^{-1} were directed to the stretching vibrations of C–O (alcohol, anhydrides, carboxylic acid, and ether) and C–H bending vibrations in aromatic compounds. The peak at 883 cm^{-1} corresponded with the C–H bending vibration of alkenes.[53] Bands can be noticed in an FTIR spectrum of TFG seed extract mediated-Co_3O_4 NPs with a slight decrease or increase in peak intensity (Fig. 3c), indicating the interaction between TFG seed extract and cobalt oxide NPs. In the FTIR spectra, a prominent absorption peak occurred at 660 cm^{-1} which is equivalent to the metal–oxygen stretching vibration, which forms the spinal structure of Co_3O_4 NPs.[54,55] The peak at 1698 cm^{-1} was the standard peak of aromatic rings as well as the in-plane bending of C═O.[45,56] These peaks revealed the production of Co_3O_4 NPs. Peaks in the 3400–3900 cm^{-1} range were attributed to the intermolecular bond of O–H stretching.[57,58] The presence of hydroxyl groups on the particle surface offers enhanced photocatalytic activity. The peak at 1698 cm^{-1} was the characteristic peak of aromatic rings and the in-plane bending of C═O.[45,56] These peaks indicated the formation of the Co_3O_4 NPs.

The peaks in the range of 3400–3900 cm^{-1} are attributed to the O–H stretching of intermolecular bonds. This O–H group is likely associated with chemically adsorbed water on the surface of Co_3O_4. Given the physical and chemical fractions of water adsorbed on Co_3O_4, the physical fraction can be disregarded because the sample was calcined at 200 °C. At this temperature, only the chemically adsorbed fraction remains. The low transmittance value suggests the presence of a significant number of OH groups on the Co_3O_4 NPs surface. A high number of hydroxyl groups on NP surfaces is known to enhance photocatalytic activity.[52] For comparison, a broad peak at

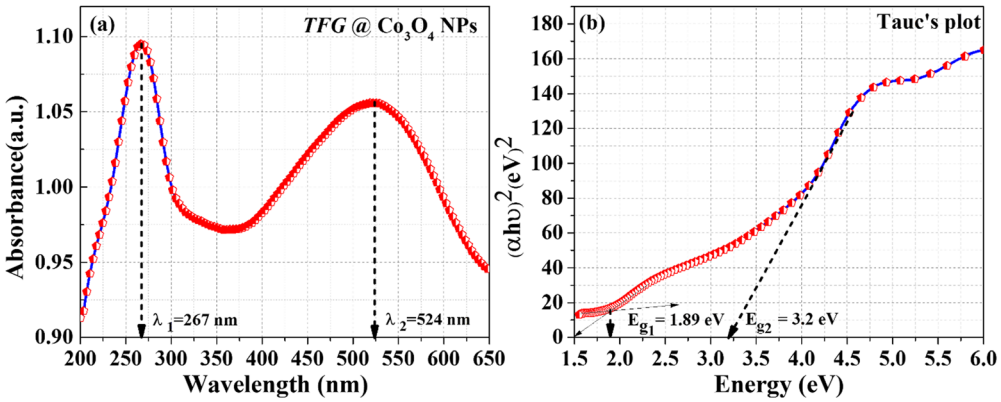

Fig. 4 UV-vis. analysis of (a) TFG-mediated Co_3O_4 NPs (b) Tauc plot of Co_3O_4 NPs.

approximately 3225 cm^{-1}, indicative of hydroxyl groups from polyphenolic compounds, was previously reported for Co_3O_4 NPs synthesized using *P. granatum* peel extract.[31]

3.3. UV-visible Analysis of TFG-Mediated Co_3O_4 NPs

By observing the UV-visible spectrum of biosynthesized Co_3O_4 NPs, the optical absorption characteristics were elucidated. Fig. 4 displays the UV-visible spectrum and Tauc plot of Co_3O_4 NPs produced by ethanolic extract of TFG seed. According to the UV-vis spectra of the sample (Fig. 4a), there is a particular absorption at two separate wavelengths in the 200–650 nm range, focused at 267 nm and 524 nm, respectively, revealing the phenolic chemicals present that are in charge of the green production of Co_3O_4 NPs. The existence of the first band close to the UV dimension, which is due to the $O^{2-} \rightarrow Co^{2+}$ charge transfer process, and the second absorption band close to the green region, which is assigned to the $O^{2-} \rightarrow Co^{3+}$ charge transfer, indicates that Co_3O_4 NPs have formed. They observed two distinct absorption peaks at different frequencies as a result of the ligand-to-metal charge transfer (LMCT) method, such as the $O^{2-} \rightarrow Co^{2+}$ charge transfer transition for the first absorption band at 267 nm and the $O^{2-} \rightarrow Co^{3+}$ charge transfer transition for the second absorption band at 524 nm, respectively.[59,60]

The UV-visible spectra of *M. charantia* leaf extract exhibit two absorption bands at 270 nm and 316 nm, as previously described. In contrast, the results of the current study are not consistent with the reported absorption bands by David *et al.*[61] when it comes to the activity of phenolic compounds that are responsible for the formation of Co_3O_4 NPs. This could be attributable to the impact of bioactive compounds found in the various plant materials employed in various research. The optical band gap of the Co_3O_4 NPs was estimated by the Tauc relation given below:[62]

$$\alpha h\gamma = A(h\gamma - E_g)^n \quad (8)$$

where A is constant, E_g is the energy band gap, and n depends on whether the transitions are direct or indirect. For the permitted direct band gap ($n = 2$), Tauc plot of $(\alpha h\gamma)^2$ *vs.* $(h\gamma)$ is drawn in Fig. 4b, and the energy band gap of the constructed sample was determined to be 1.89 eV and 3.2 eV, respectively, the values are considerably higher than the one that is reported in the literature for bulk Co_3O_4 and Co_3O_4 nanomaterials.[45,63–65]

In a recent investigation, values of bandgap of 3.35 eV and 3.18 eV have been reported using *Phytolacca dodecandra* leaf extract and chemically synthesized Co_3O_4 NPs, respectively.[66] A previous study reported an E_g value of 3.4 eV for Co_3O_4 NPs synthesized through the auto-combustion method with fresh *lemon* juice with heat treatment at 350 °C.[67] Similarly, an E_g value of 3.4 eV was reported for Co_3O_4 NPs synthesized using *Curcuma longa* leaf extract.[49] In this context, the organic components present in TFG seed extract are likely to exert superior control over the optical properties, resulting in a smaller E_g value. As a result, the synthesized Co_3O_4 NPs are expected to exhibit enhanced photocatalytic performance in the UV-visible range.

Thus, the UV-visible analysis of TFG-mediated Co_3O_4 NPs revealed unique absorption peaks, with a prominent peak observed in the visible region. The electronic transitions within the Co_3O_4 NPs are responsible for the position and intensity of the absorption peaks. The observed absorption behavior underscores the distinctive optical characteristics conferred by the TFG-mediated synthesis method. The existence of a prominent absorption band in the visible area suggests that the nanoparticles have the potential to be used in visible-light-driven catalysis or photocatalysis. The absorbance characteristics of the TFG-mediated Co_3O_4 NPs are consistent with their crystalline structure and purity, as validated by supplementary tests such as X-ray diffraction. Furthermore, the UV-visible analysis provides critical information about the bandgap of the synthesized Co_3O_4 NPs, revealing their electronic structure. This knowledge is critical for comprehending the reactivity of nanoparticles and their prospective uses in photovoltaics, sensors, and other optoelectronic devices. In conclusion, UV-visible analysis has been useful in characterizing the optical characteristics of TFG-mediated Co_3O_4 nanoparticles, revealing information on their prospective uses in a variety of domains, including photocatalysis and optoelectronics.

3.4. Morphology and elemental analysis

Scanning electron microscopy was used to analyze the morphology of the produced nanoparticles. Fig. 5a and b exhibit

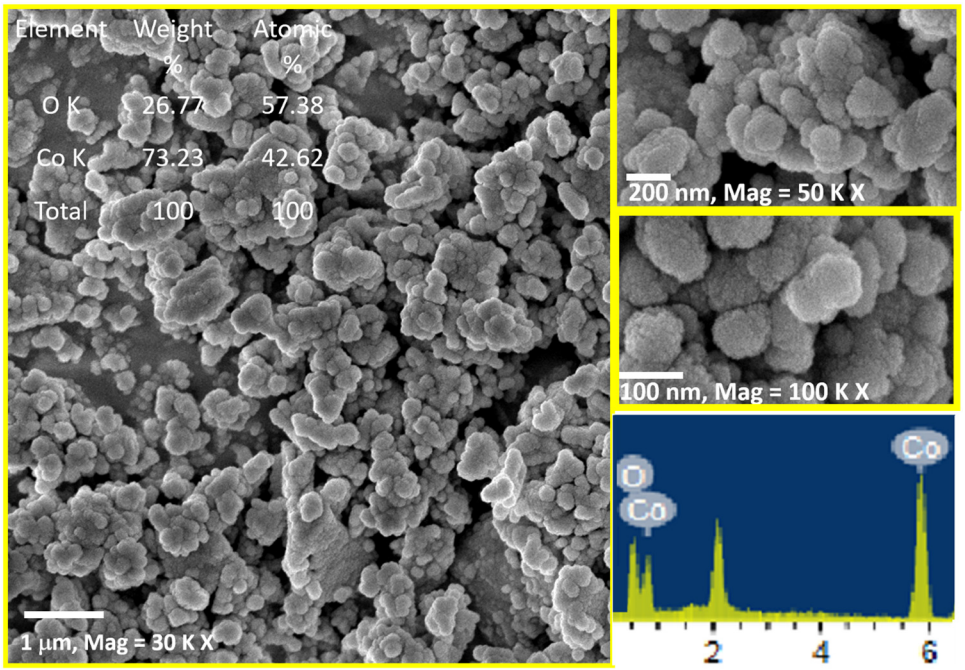

Fig. 5 FESEM images of green synthesized Co_3O_4 NPs at different magnifications: (a) at 30 000 (b) at 50 000, (c) at 100 000 magnifications, and (d) EDX spectrum.

the surface morphology of TFG-mediated Co_3O_4 NPs at various magnifications. Individual Co_3O_4 NP agglomerations can be observed in the SEM images. A deeper examination of these aggregated pictures reveals that some of the particles are semi-spherical (Fig. 5a), while a few are monoclinic non-spherical (Fig. 5b). The formation of the sphere-like shape of Co_3O_4 NPs can be shown in Fig. 5c.

The elemental composition of the synthesized tricobalt tetra-oxide nanoparticles was determined using an energy-dispersive X-ray diffractive (EDX) analysis. The energy dispersive spectra (EDS) of the prepared sample showed that the sample generated by the above method contains pure Co_3O_4 phases. As shown in Fig. 5d, EDX validates the presence of cobalt and oxygen signals in cobalt oxide nanoparticles, and this analysis revealed the peaks that matched the optical absorption of the generated nanoparticle. The optical absorption peaks of Co_3O_4 NPs are seen in the EDS analysis, and these absorption peaks are caused by the surface plasmon resonance of cobalt oxide nanoparticles. These elements are derived from biological components, namely alga and Co_3O_4 NPs. The elemental analysis of the nanoparticle revealed 73.23% cobalt and 26.77% oxygen, indicating that the created nanoparticle is in its purest form. The EDX experiments yielded equivalent findings to previous work, with elemental analysis of the nanoparticle providing 59.27% cobalt and 40.73% oxygen reported by Nagal *et al.* in 2023, whilst Marimuthu *et al.* reported weight of 67.56% cobalt and 32.44% oxygen in 2020.[68,69]

The FESEM analysis revealed that TFG functional groups appear to create a distinct coating around the Co_3O_4 NPs. This suggests that TFG might be more effective than other green extracts in minimizing NP aggregation and achieving better size control. Further investigation is needed to fully understand the mechanisms by which TFG interacts with the NPs and influences their morphology.

3.5. Transmission electron microscopy

Transmission electron microscopy (TEM) serves as an indispensable tool, providing profound insights into the dimensions, configuration, and crystalline composition of nanomaterials. In the context of this research, we employed both high-resolution TEM (HRTEM) and selected area electron diffraction (SAED) techniques to precisely characterize the morphological attributes and crystallinity of Co_3O_4 NPs synthesized through a TFG-mediated approach. Fig. 6 provides a comprehensive analysis of TFG-mediated Co_3O_4 NPs, utilizing high-resolution transmission electron microscopy (HRTEM), a size distribution histogram, fringe patterns, and selected area electron diffraction (SAED) patterns. The aggregates of TFG-mediated Co_3O_4 NPs depicted in Fig. 6(a) find support in the literature, where similar aggregation phenomena have been observed in the bio-mediated synthesis of metal oxide nanoparticles.[70,71] The size distribution histogram (Fig. 6b) and the average particle size of 5.5 nm are indicative of controlled synthesis, a phenomenon attributed to the influence of phytochemicals in TFG. This is consistent with the findings of Zuhrotun *et al.* (2023), who reported that the phytochemicals present in plant extracts act as effective capping agents, regulating the size and morphology of nanoparticles during biosynthesis.[72]

Phytochemicals within TFG, including compounds such as saponins and polyphenols, emerge as proficient capping agents in the Co_3O_4 NPs synthesis.[73] These molecules form a protective sheath around the nascent nanoparticles, acting as molecular guards that thwart unbridled growth and aggregation. This capping prowess is fundamental in conferring a distinct and uniform size distribution to the nanoparticles,

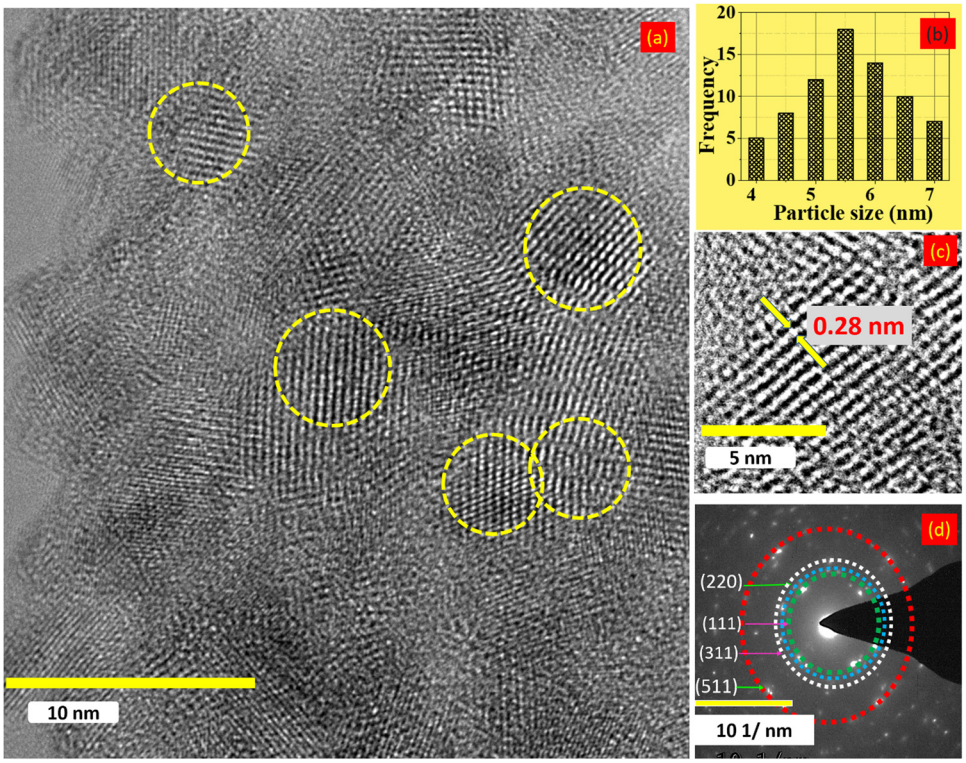

Fig. 6 Morphological exploration of TFG-mediated Co_3O_4 NPs: (a) TEM image, (b) particle size distribution, (c) *d*-spacing HRTEM, and (d) SAED pattern.

as discerned from the accurately illustrated histogram. Flavonoids and alkaloids found in TFG's chemical repertoire serve as stalwart stabilizing agents.[74] Their presence is pivotal in curbing the tendency of NPs to coalesce or agglomerate, ensuring the stability of the nanoparticle dispersion. This stability, governed by the chemical balance struck by these phytochemicals, is paramount for maintaining the individual identity of nanoparticles and guarding against undesirable alterations in size or shape over temporal scales.

Phytochemicals, notably terpenoids, and tannins, actively engage in the reduction and nucleation phases of nanoparticle synthesis. Their intervention in the reduction kinetics and nucleation processes orchestrates a delicate control mechanism, influencing the initiation and subsequent growth of Co_3O_4 NPs. The discernible outcome is the meticulous formation of NPs within a specific size range, a manifestation exemplified by the average particle size of 5.5 nm. The dynamic interplay between TFG phytochemicals, such as coumarins and sterols, and the nanoparticle surface plays a pivotal role in shaping crystal growth and morphology. These surface interactions serve as molecular orchestrators, guiding the arrangement of atoms during the crystal growth phase. The result is prominently displayed in the HRTEM micrograph, where well-defined lattice fringes bear witness to the highly crystalline nature of the nanoparticles. TFG's phytochemical composition, including compounds like alkaloids and saponins, assumes the role of biological templates in the formation of Co_3O_4 NPs. The inherent chemical blueprint of these compounds provides a template for the nucleation and subsequent growth of nanoparticles, imparting a specific morphology. This templating effect is notably evident in the observed spherical shape of the nanoparticles, a testament to the guiding influence of TFG's chemical constituents in the nanomaterial synthesis process. The well-resolved lattice fringes observed in the HRTEM micrograph (Fig. 6c) align with the literature on crystallinity analysis. The study by Hirpara *et al.* (2022) and Mourdikoudis *et al.* (2018)[75,76] demonstrated that lattice fringes in HRTEM images are crucial for determining the crystalline nature of nanoparticles and extracting information about interplanar spacings. The distinctive d-spacing of 0.28 nm, indicative of atomic planes in Co_3O_4, is consistent with known values reported in the literature.[57,77]

At 500 KX magnification, the HRTEM provides an intricate view into the crystallinity of TFG-mediated Co_3O_4 NPs, unveiling a captivating narrative supported by empirical evidence. The captured image vividly presents well-defined lattice fringes, serving as a visual testament to the exceptional crystalline nature of the synthesized material. This observation aligns with established literature emphasizing HRTEM's capability to reveal nanoscale features with remarkable precision.[78] The discernible lattice fringes in the HRTEM micrograph disclose a characteristic *d*-spacing of 0.28 nm, a key feature indicative of atomic planes in Co_3O_4. This finding is consistent with known values reported in the literature, as demonstrated by the study conducted by Al Jahdaly *et al.* (2022)[57] highlighting the significance of lattice fringes in HRTEM images for determining the crystalline nature of nanoparticles and extracting information about interplanar spacings. Of particular significance is the

presence of singular, isolated crystallites within the TFG-mediated Co_3O_4 NPs, serving as a compelling confirmation of their monocrystalline nature. This observation not only reinforces the precision of the synthesis process but also contributes to the broader understanding of the material's structural intricacies. Each crystallite emerges as a miniature masterpiece, characterized by an ordered arrangement of atoms, as corroborated by existing research on monocrystalline nanoparticles.[79] In essence, the detailed examination at 500 KX magnification through HRTEM not only unravels the crystalline nature of TFG-mediated Co_3O_4 NPs but also provides valuable insights that contribute to the scientific understanding of their structural intricacies, reinforcing the significance of employing advanced microscopy techniques in nanomaterial characterization.

3.6. X-ray photoelectron spectroscopy (XPS)

XPS is a powerful analytical technique that plays a pivotal role in unravelling the chemical composition and oxidation states of elements residing on the surface of materials. In the context of this investigation, XPS is employed as a key tool to illuminate the intricate surface chemistry of Co_3O_4 NPs synthesized through a TFG-mediated approach. The detailed findings are depicted in Fig. 7, providing a comprehensive view of the elemental and chemical landscape of these nanoparticles. The survey spectrum (Fig. 7a) in XPS reveals crucial information about the elemental constituents of TFG-mediated Co_3O_4 NPs. The distinct peaks in the spectrum unequivocally showcase the presence of cobalt (Co), carbon (C), and oxygen (O). Specific binding energies are employed to precisely pinpoint the location of various Co species, including Co 2s at 926.90 eV, Co $2p_{1/2}$ at 837.1 eV, and Co $2p_{3/2}$ at 775.66 eV. Additional peaks corresponding to O 1s (530.24 eV) and C 1s (284.60 eV) further consolidate the elemental composition of the Co_3O_4 NPs.

Fig. 7b provides a closer examination through the high-resolution Co 2p spectrum, offering deeper insights into the chemical environment of cobalt within the nanoparticles. The characteristic doublet structure of Co $2p_{1/2}$ and Co $2p_{3/2}$ reveals distinct peaks. The Co $2p_{3/2}$ peak at 779.43 eV signifies the presence of Co^{3+} in Co_3O_4, while the Co $2p_{1/2}$ peak at 794.24 eV corroborates the formation of CoO NPs. The observation of intense satellite peaks further suggests the coexistence of Co ions in the +2 and +3 oxidation states. Importantly, the absence of a peak at 777.10 eV confirms the absence of metallic cobalt impurities, aligning with complementary analyses such as XRD and SAED. Some studies using hydrothermal or solvothermal methods report the presence of mixed oxidation states (+2 and +3) alongside metallic cobalt impurities.[80] In contrast, our XPS results for TFG-mediated Co_3O_4 NPs showcase a well-defined coexistence of Co^{3+} and Co^{2+} without any detectable metallic cobalt peaks. This suggests a superior control over the oxidation state and purity achieved through the TFG-mediated

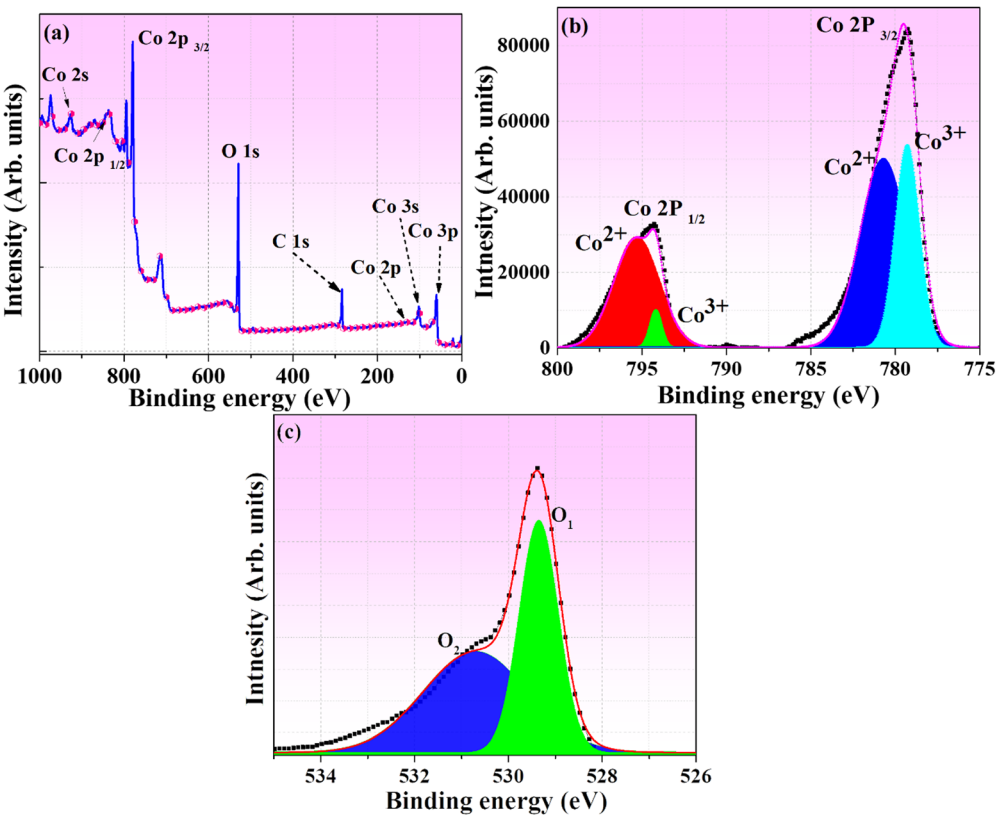

Fig. 7 XPS analysis of Co_3O_4 NPs: (a) Holistic elemental survey (b) cobalt chemical environment – Co 2p spectra, and (c) oxygen's role in Co_3O_4 Structure – O 1s Spectra.

synthesis, potentially leading to enhanced properties for specific applications. In Fig. 7c, the high-resolution O 1s spectrum is presented, deconvoluted into three peaks to provide a nuanced understanding of oxygen's role in the Co_3O_4 structure. The dominant O_1 peak at 529.34 eV signifies oxygen integrated into the Co_3O_4 structure through metal-oxygen bonds. The broader O_2 peak at 530.82 eV indicates defect sites with lower oxygen coordination, as reported by Zhang *et al.*[81] These peaks collectively confirm the successful formation of Co_3O_4 NPs, with oxygen atoms bonded to both cobalt and other oxygen atoms.

In essence, XPS serves as a valuable tool in uncovering the surface composition and oxidation states of TFG-mediated Co_3O_4 NPs, providing essential insights that contribute to a deeper understanding of their properties and potential applications in various fields, including catalysis, energy storage, and biomedical applications. Further research avenues may involve theoretical calculations to validate XPS findings and explore the influence of TFG phytochemicals on the surface characteristics of these nanoparticles.

3.7. Photocatalytic analysis

Photocatalysis, the sun-driven engine for unlocking efficient and sustainable chemical reactions, offers immense potential for environmental remediation.[82] This work delves into this exciting field, exploring the fascinating capabilities of newly synthesized TFG-mediated Co_3O_4 NPs in promoting the breakdown of the notoriously persistent Congo Red (CR) dye. Congo Red's alluring appeal lies in its vibrant red color, a signature characteristic of azo dyes. This captivating hue originates from the robust –N═N– chromophore group, a molecular bridge connecting two aromatic rings (Christie, 2003; Zollinger, 2003). Beyond its aesthetic charm, this intricate structure imbues CR with remarkable stability, making it highly resistant to degradation. These unique properties elevate CR to a formidable benchmark for evaluating the efficacy of photocatalysts. To comprehensively assess the performance of our Co_3O_4 NPs, we establish a crucial baseline by examining the behavior of CR under UV light in the absence of any catalyst (Fig. 8a). This initial exploration provides a null reference point, allowing us to precisely quantify the enhanced degradation facilitated by our TFG-mediated Co_3O_4 NPs when introduced to the system.

Interestingly, under UV light exposure alone for 80 minutes, CR dye displayed remarkable stability, with its concentration and vivid color remaining virtually unchanged. This resilience underscored the limitations of UV light alone in effectively degrading persistent dyes. However, the introduction of our synthesized TFG-mediated Co_3O_4 NPs as photocatalysts marked a crucial turning point in the experiment (Fig. 8b). In stark contrast to the UV-only scenario, CR encountered a formidable adversary. Its vibrant hues swiftly succumbed to degradation, and its concentration significantly plummeted within the same 60-minute timeframe. This notable decline serves as compelling

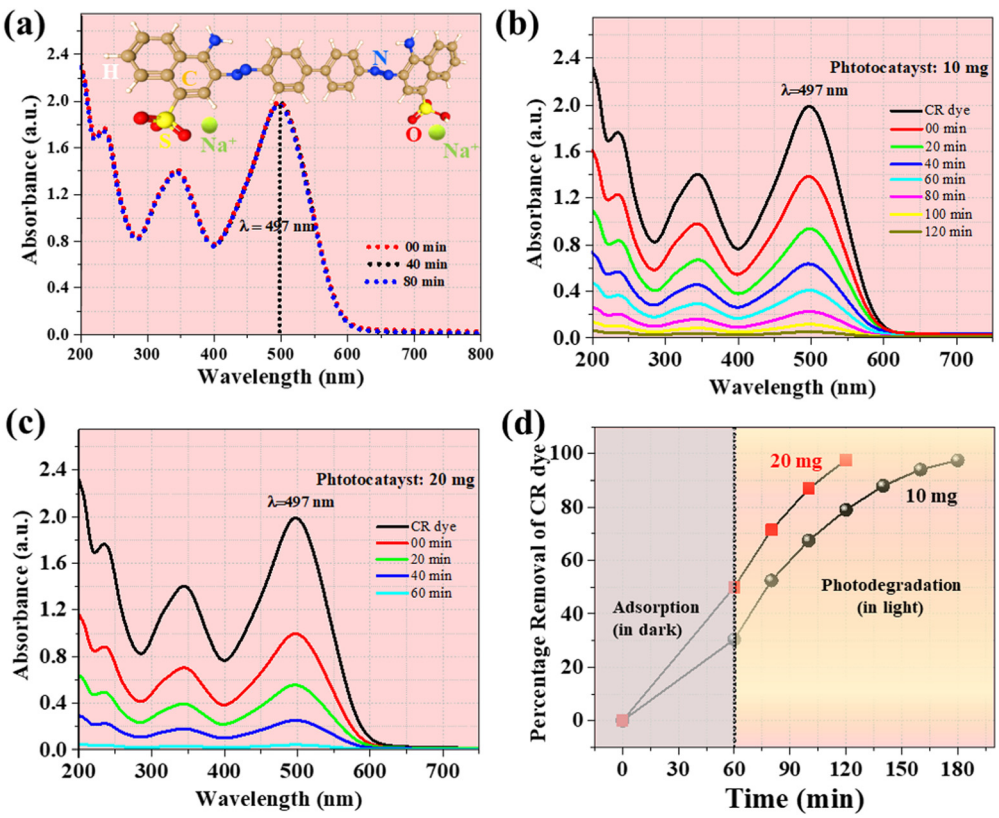

Fig. 8 Photodegradation of CR dye using Co_3O_4 NPs.

evidence for the exceptional efficacy of TFG-mediated Co_3O_4 NPs in cleaving the intricate aromatic rings constituting CR's robust backbone.

The outstanding performance of our TFG-mediated Co_3O_4 NPs can be ascribed not only to their inherent photocatalytic properties but also to the pivotal role played by TFG phytochemicals employed in their synthesis. These bioactive molecules contribute to the enhanced performance in several key ways: (a) morphology guidance: TFG phytochemicals act as surfactants, influencing the growth and shape of the Co_3O_4 NPs during synthesis.[83] This influence can lead to the formation of specific crystal facets with higher photocatalytic activity due to their increased surface area and exposure to active sites. (b) Nanoparticle Stabilization: TFG molecules coat the surface of Co_3O_4 NPs, preventing aggregation and agglomeration. This coating improves their dispersion in the reaction medium and increases their availability for interacting with dye molecules, thereby boosting the overall reaction rate.[84] (c) Enhanced charge separation: TFG molecules can modify the electronic structure of Co_3O_4 NPs, facilitating the separation of photogenerated electrons and holes.[85] This separation minimizes recombination losses, allowing the charges to participate in subsequent redox reactions with the dye molecules and improving the efficiency of the photodegradation process and (d) photoinduced electron transfer: the positive charge of the TFG head group attracts negatively charged dye molecules to the Co_3O_4 surface, promoting close contact, and enhancing the transfer of photoexcited electrons from the dye to the Co_3O_4 conduction band. This initiation of the degradation process of the dye molecule.[86] Therefore, TFG phytochemicals play a multifaceted role in enhancing the photocatalytic performance of Co_3O_4 NPs by influencing their morphology, stabilizing their dispersion, improving charge separation, and facilitating electron transfer. This synergistic effect translates to the remarkable breakdown of CR dye observed in our study.

Fig. 8(b)–(d) research the photocatalytic prowess of our TFG-mediated Co_3O_4 NPs against CR under various conditions. Encompassing both darkness and UV light exposure at different NP dosages (100 and 200 mg L^{-1}), these analyses illuminate the dynamic dance between catalyst concentration and degradation efficiency. A consistent decline in CR concentration over time is evident across all scenarios, manifested by the diminishing peak at 497 nm in the UV-Vis spectra. However, the tempo quickens under UV irradiation, particularly at the higher NP dosage. With 100 mg L^{-1} of NPs, a remarkable 79% drop in the peak is observed after just 60 minutes, signifying extensive dye degradation (Fig. 9(b)). This accomplishment is further echoed by the mesmerizing transformation of the solution, its vibrant red hue yielding to pristine transparency – a testament to the thorough dismantling of the CR molecule.

Fig. 8(c) sheds light on the pivotal role played by Co_3O_4 NP concentration in this intricate symphony. At higher dosages (200 mg L^{-1}), a greater density of active sites graces the NP surface, effectively acting as magnet-like attractants for CR molecules. Conversely, at lower concentrations, the scarcity of active sites can bottleneck the process, imposing mass transfer limitations that impede dye molecules' access.[87] Boosting the NP concentration overcomes these limitations by narrowing the average distance between dye molecules and active sites, resulting in a smoother, more efficient transfer of reactants.[88] This optimization transcends mere mass transfer, igniting a synergistic interplay that propels the degradation rate to dizzying heights. Increased adsorption elevates the probability of a CR molecule encountering an active site, while the abundance of available sites ensures a readily accessible pool of charge carriers for immediate degradation reactions.[89] This dynamic cooperation culminates in a significantly accelerated degradation rate, culminating in complete dye removal at the 200 mg L^{-1} dosage. This potent combination becomes the key conductor in the orchestra of breakdown at higher NP concentrations.

These profound insights illuminate the delicate interplay between NP concentration and degradation efficiency. Optimizing the dosage plays a critical role in achieving peak performance, ensuring the ideal balance between the dance of nanoparticles

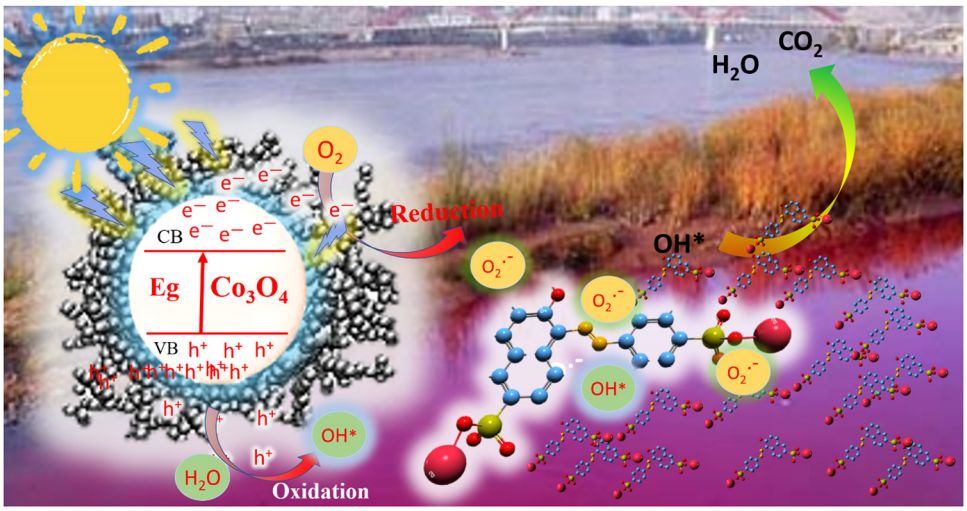

Fig. 9 Proposed photocatalytic degradation mechanism of Co_3O_4 NPs.

and CR molecules. By understanding this delicate orchestration, we unlock the full potential of Co_3O_4 NPs as potent photocatalysts for environmental remediation.

3.7.1. Mechanisms of TFG-mediated Co_3O_4 NPs in degradation of CR dye. The remarkable ability of TFG-mediated Co_3O_4 nanoparticles to efficiently catalyze the degradation of CR dye is attributed to a complex interaction of processes resulting from the synergistic effect between the nanoparticles and the integrated phytochemicals (Fig. 9). When exposed to UV radiation, the Co_3O_4 nanoparticles capture light, causing the electrons to move from the valence band to the conduction band and creating pairs of electrons and holes.[90] TFG phytochemicals significantly influence these photocatalytic processes *via* many crucial mechanisms: (a) improved charge separation: the electrically charged parts of TFG molecules work as very effective electron acceptors, efficiently trapping photoexcited electrons from the Co_3O_4 conduction band, surpassing the effectiveness of conventional surfactants such as CTAB.[91]

The fast transport of electrons reduces the occurrence of electron–hole recombination, hence extending the lifetime and enhancing the presence of very reactive charge carriers for later degradation events.[92] (b) Production of reactive oxygen species (ROS): the TFG molecules grab electrons which then interact with dissolved oxygen, triggering the creation of powerful ROS such as superoxide and hydroxyl radicals.[90] These extremely reactive species have a crucial function in chemically attacking and breaking down the organic dye molecules, specifically targeting the azo linkages and aromatic rings included in CR's structure.[93] (c) Direct hole oxidation: the residual vacancies in the Co_3O_4 valence band engage in direct oxidation reactions with CR molecules that have been adsorbed onto the surface of the catalyst. The holes in this frontal assault efficiently disrupt the azo link and aromatic rings present in the dye molecule, therefore commencing its disintegration into smaller organic pieces. (d) Enhanced adsorption and electron transfer: the polar functional groups and aromatic rings present in TFG phytochemicals engage in hydrophobic and electrostatic interactions with dye molecules, hence facilitating their effective adsorption onto the surface of Co_3O_4. The close closeness between dye molecules and the Co_3O_4 conduction band improves the efficiency of electron transport, hence speeding up the degradation process.[94] (e) Enhanced stability and dispersion: unlike most artificial surfactants, TFG molecules often display amphiphilic characteristics, acting as stabilizers for Co_3O_4 NPs in the reaction media. This hinders the accumulation and clustering of particles, guaranteeing enhanced scattering and availability of reactive sites for interacting with dye molecules, consequently enhancing the overall efficiency of photocatalysis.[95] (f) Precise selectivity of azo bonds: specific functional groups in TFG phytochemicals exhibit preferential interaction with the azo bond found in CR molecules. The precise targeting in question improves the efficiency of degradation by directly triggering the breaking of chemical bonds and impeding the reformation of polymers throughout the process.[96] At last, molecules of CR dye were degraded to H_2O, CO_2, and other harmless molecules.[90]

Essentially, TFG-mediated Co_3O_4 NPs act as a precisely controlled photocatalytic system, where phytochemicals coordinate important processes to achieve effective degradation. These biomolecules interact together to increase the breakdown of the persistent dye by enhancing charge separation, generating reactive oxygen species (ROS), facilitating adsorption, increasing stability, and specifically targeting the azo bond of the dye. The complex interaction shown here emphasizes the possibility of using natural extracts like TFG as sustainable and efficient substitutes for manufactured surfactants in photocatalytic applications aimed at treating organic pollutants like CR.

3.7.2. Investigation of CR degradation kinetics. The photocatalytic degradation of CR dye has been systematically studied at a fixed concentration of 120 mg L^{-1}, employing varying doses of the photocatalyst (TFG-mediated Co_3O_4) at 100 and 200 mg L^{-1} (Fig. 10). To elucidate the reaction kinetics, pseudo-zero-order, pseudo-first-order, and pseudo-second-order kinetic plots are made using the provided equations, and pertinent parameters are extracted.[97]

Zero-order kinetics. In zero-order kinetics, the reactant concentration diminishes linearly with time, irrespective of its initial concentration. The equation is represented as:

$$C_t = C_0 - k_0 \times t \quad (9)$$

First-order kinetics. In first-order kinetics, the reaction rate is directly proportional to the concentration of the reactant, expressed as:

$$\ln(C_t) = \ln(C_0) - k_1 \times t \quad (10)$$

Second-order kinetics. Second-order kinetics states that the reaction rate is proportional to the square of the reactant concentration. The equation is written as:

$$1/C_t = 1/C_0 + k_2 \times t \quad (11)$$

In these equations, k_0, k_1, and k_2 denote the rate constants for zero-order, first-order, and second-order kinetics, respectively. The rate constant values specific to CR degradation are provided in Table 2. Evaluation of the regression coefficients (R^2) indicated that the pseudo-first-order kinetic model ($\ln(C_0/C_t)$ *vs.* irradiation time) best fits the CR degradation pattern (Fig. 10(b)). This suggests a direct proportionality between the degradation rate and the remaining CR concentration. Observing the kinetic results, the reaction-rate constant substantially increases from 0.02698 min^{-1} to 0.05049 min^{-1} as the Co_3O_4 dose escalates from 10 mg to 20 mg. This underscores the enhanced performance of the 20 mg photocatalyst. Even after five cycles of reusability, the photocatalyst retains its effectiveness, removing more than 90% and 85% of CR dye at concentrations of 200 mg L^{-1} and 100 mg L^{-1}, respectively (Fig. 10(d)). Notably, these results surpass reported photocatalytic outcomes in the literature, emphasizing the superior

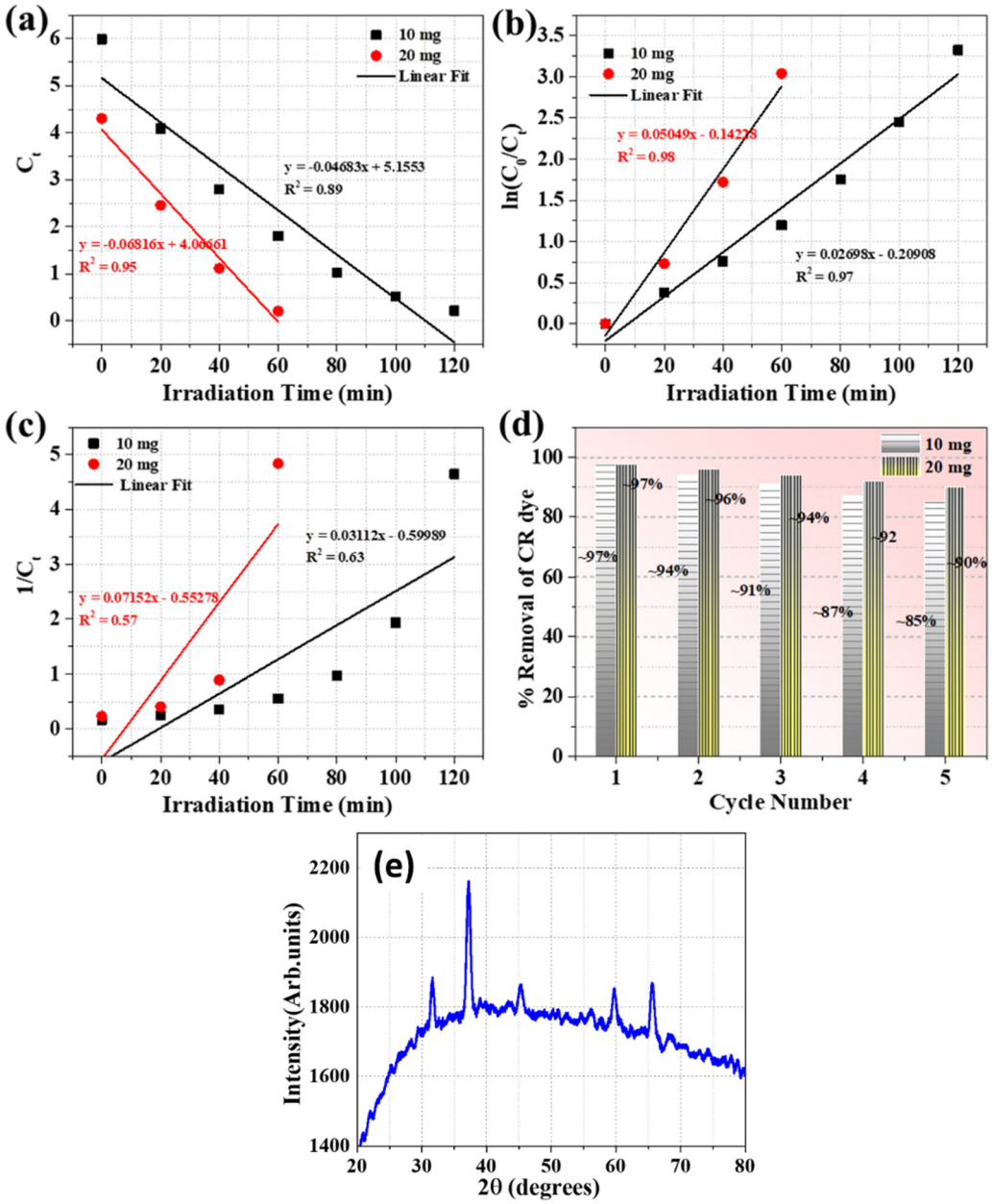

Fig. 10 Kinetics of CR dye: (a) Pseudo-zero-order, (b) Pseudo-first-order, and (c) Pseudo-second-order, (d) reusability of TFG-Co_3O_4, and (e) stability of TFG-Co_3O_4.

Table 2 Reaction rates and regression coefficients for degradation of CR dye

S. no.	Catalyst dose (mg L^{-1})	Pseudo-zero-order		Pseudo-first-order		Pseudo-second-order	
		k_0 (mg L^{-1} min^{-1})	R^2	k_1 (min^{-1})	R^2	k_2 (L mg^{-1} min^{-1})	R^2
1	100	0.04683	0.89	0.02698	0.97	0.03112	0.63
2	200	0.06816	0.95	0.05049	0.98	0.07152	0.57

efficiency of the synthesized Co_3O_4 (Table 2). The stability of the synthesized TFG-Co_3O_4 nanoparticles was confirmed by XRD analysis conducted after the photocatalytic degradation of CR dye, which showed no significant change in the crystalline structure, indicating that the nanoparticles maintain their structural integrity during and after the catalytic process (Fig. 10(e)).

3.7.3. Comparison of photocatalytic results with literature. The present study demonstrates a significantly higher photocatalytic removal efficiency compared to previous studies, as

Table 3 Comparison of present photocatalytic results with previous reports

S. no.	PC	Synthesis method	Dye	PC dose	Light source	RE (%)	Time (minutes)	Ref.
1	CoO	Green	AB74	20 mg	UV	98	150	98
2	Co_3O_4	Green	RBO	500 mg	Solar	78	50	31
3	Co_3O_4	Green	McG	50 mg	Simulated sunlight	91	100	99
4	Co_3O_4	Green	CR	30 mg	Visible	96	240	65
5	Co_3O_4	Green	DB71	20 mg	UV	79	80	102
6	Co_3O_4	Green	MR	125 μg mL^{-1}	Sunlight	53	360	103
			MO			56	360	
7	Co_3O_4	Green	CR	20 mg	UV	98	60	Present study
8	Fe_3O_4	Green	IC	5 mg	Visible	77.9	180	104
			BG			80.4		
			MR			73.9		
9	ZnO-60 ZnO-RT	Green	CBB	—	UV	80	60	105
10	ZnO	Green	MO	75 mg L^{-1}	UV	87	270	106
11	ZnO	Green	MR	50 mg	Solar	99	180	100
12	TiO_2	Green	CR	20 mg	UV	97	150	101
13	TiO_2	Green	RG	20 mg	UV	96	180	107
14	CuO	Green	CR	50 mg	Sunlight	90	60	108
15	CuO	Green	MB	100 mg	Sunlight	71	200	109
16	CuO	Electro-chemical	CR	10 mg	Sunlight	85	120	110
			MB			93		
17	CuO	Mechano-chemical	MG	10 mg	Sunlight	65	60	111
			MO			65		

Note: PC: Photocatalyst, AB: Acid blue, RBO: remazol brilliant orange, McG: malachite green, DB: direct blue, MR: methyl red, MO: methyl orange, IC: indigo carmine, BG: brilliant green, CBB: coomassie brilliant blue, RG: reactive green, MB: methylene blue, MG: methyl green, RE: removal efficiency.

summarized in Table 3. The present photocatalyst, Co_3O_4, synthesized using a green method, achieved a 98% removal efficiency of CR dye in just 60 minutes under UV light. This performance is notably superior to other reported studies utilizing similar conditions and materials. CoO synthesized *via* a green method removed 98% of Acid Blue 74, but it required 150 minutes under UV light.[98] Additionally, Co_3O_4 synthesized through the green method showed a 91% removal of Malachite Green under simulated sunlight, but it took 100 minutes.[99] Other studies with Co_3O_4 also reported lower removal efficiency and longer durations, such as the 96% removal of CR in 240 minutes using visible light[65] and a 78% removal of Remazol Brilliant Orange in 50 minutes under solar light.[31] Moreover, ZnO-based photocatalysts exhibited varied efficiencies depending on dye and conditions; for example, ZnO achieved a 99% removal of Methyl Red in 180 minutes under solar light,[100] but this took significantly longer than our study. TiO_2 photocatalysts also showed high efficiencies, such as 97% removal of CR under UV light in 150 minutes,[101] but still required more time compared to our findings.

Thus, the present study stands out due to its remarkable photocatalytic activity, achieving near-complete dye degradation in a shorter time frame than most of the previously reported photocatalysts, underlining its potential for efficient environmental remediation applications. While the study demonstrates the efficacy of TFG-mediated Co_3O_4 nanoparticles in degrading Congo Red dye, the photocatalytic performance was tested only under specific conditions (UV irradiation, concentration of 120 mg L^{-1}). Future studies could explore the efficiency of these nanoparticles across a broader range of environmental conditions, including varying pH levels, different light sources (*e.g.*, visible light), and other dye pollutants to validate the generalizability of the results.

3.7.4. Investigation of the degraded fragmentation products of CR dye *via* GC-MS. The metabolites released during the breakdown of CR dye by TFG-Co_3O_4 NPs under UV irradiation were identified using the GC-MS analysis (Fig. 11). There were multiple peaks in the GC of the degraded dye metabolites, but only the distinctive peaks at *m/z* 418, 245, 207, and 137 have been associated with the degradation products A–D. Fig. 11 suggests the structure of the detected compounds based on the fragmentation pattern as well as the entire fragmentation pattern. The GC-MS results are consistent with the formation of salicylic acid and benzidine as the breakdown metabolites with the lowest molecular weights, which further degrade into harmless compounds.

3.8. Antibacterial efficacy of TFG-mediated Co_3O_4 NPs against *P. aeruginosa* and *S. aureus*

The antibacterial efficacy of TFG-mediated Co_3O_4 NPs against both Gram-negative *Pseudomonas aeruginosa* and Gram-positive *Staphylococcus aureus* was systematically investigated using the agar well diffusion technique (Fig. 12).

In this experimental setup, Nutrient Broth (NB) medium obtained from HiMedia Laboratories was chosen as the growth medium for the bacterial cultures and the agar plates. Rigorous sterilization of both the media and plates was achieved through autoclaving at 121 °C for 15 minutes. Post-sterilization, 20 mL of autoclaved NB medium was carefully dispensed into sterilized Petri dishes and allowed to solidify, providing a stable substrate for bacterial growth. Cultures of *P. aeruginosa* and *S. aureus* were meticulously prepared in NB broth. Subsequently,

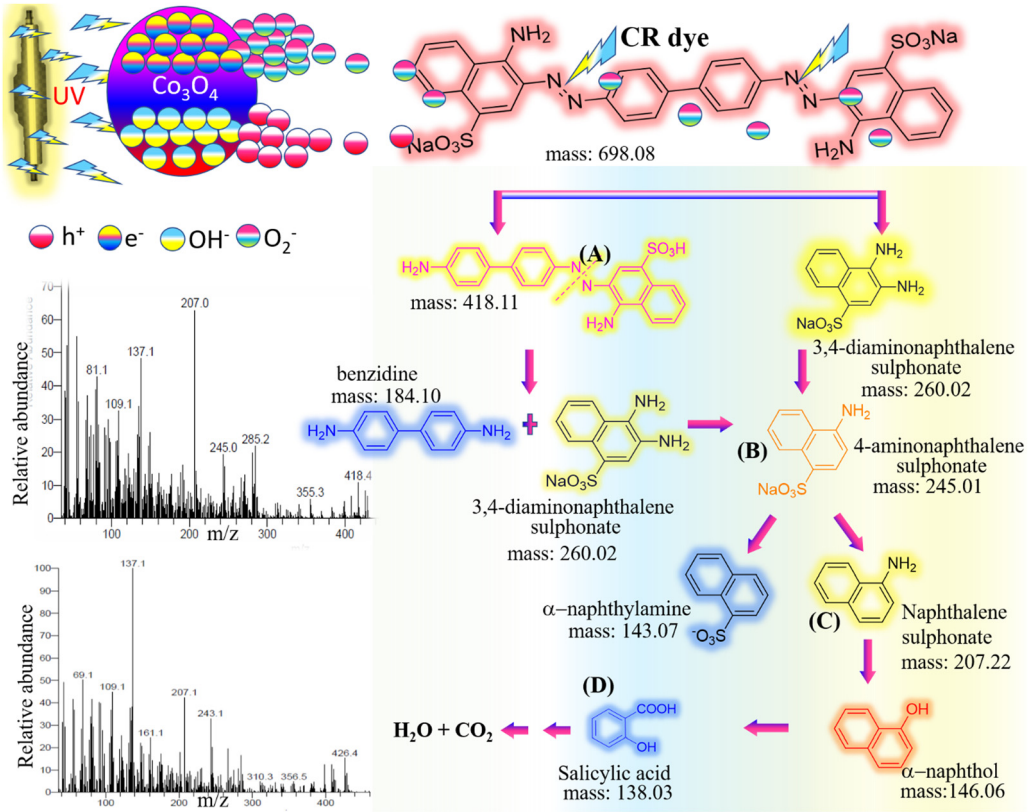

Fig. 11 The GC-MS predicted fragmentation pattern of CR dye photodegradation in the presence of bio-active CP-Co_3O_4 NPs.

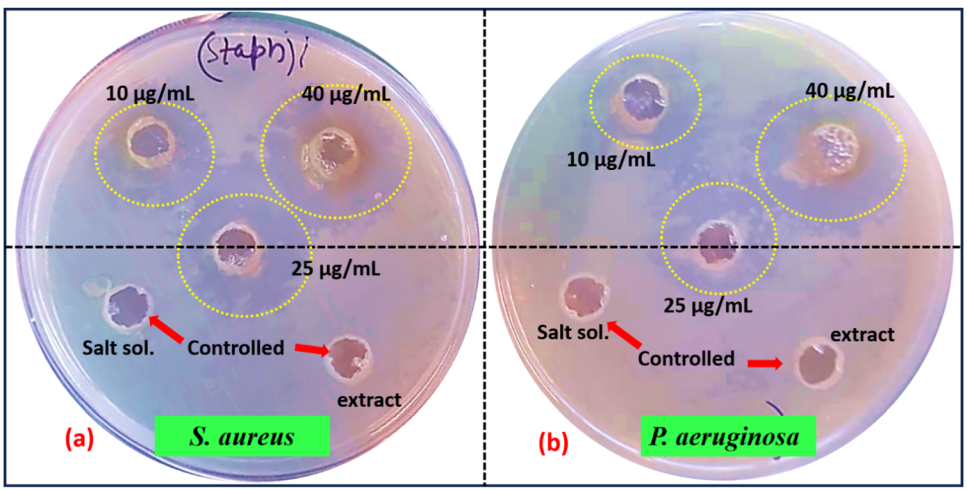

Fig. 12 Antibacterial activity of TFG-mediated Co_3O_4 NPs.

aliquots from each culture were separately inoculated onto NB agar plates, followed by a 24-hour incubation period at 37 °C with continuous shaking at 80 RPM. After incubation, bacterial cultures were diluted to a standardized cell density of 1 : 100 in fresh NB medium. Sterilized well borers were then employed to create wells in the solidified NB agar plates already seeded with bacteria. Distinct volumes (*e.g.*, 10, 25, 40 µg mL^{-1}) of the TFG-mediated Co_3O_4 NPs solution were accurately pipetted into the respective wells. To serve as controls, solutions such as sterile water or TFG suspension without NPs may have been included for comparative analysis. The plates underwent a subsequent incubation period of 24 hours at 37 °C. Finally, the diameters of the clear zones surrounding the wells, indicative of inhibition zones, were accurately measured and recorded in Table 4. This systematic assessment provides crucial insights into the antibacterial potential of TFG-mediated Co_3O_4 NPs at varying concentrations against the

Table 4 Zone of inhibition (ZOI) of TFG-mediated Co_3O_4 NPs against *P. aeruginosa* and *S. aureus*

S. no.	Bacteria	ZOI (mm) at different concentrations		
		10 μg mL^{-1}	25 μg mL^{-1}	40 μg mL^{-1}
1	*S. aureus*	11.8	23.2	26.6
2	*P. aeruginosa*	8.0	13.4	19.6

tested bacterial strains, contributing to the understanding of their practical applications in microbial control and biomedical fields.

3.8.1. Antibacterial activity against *S. aureus* and *P. aeruginosa*. The antimicrobial efficacy of TFG-mediated Co_3O_4 NPs against both Gram-positive *S. aureus* and Gram-negative *P. aeruginosa* is illustrated in Fig. 13, presenting a multifaceted attack mechanism. The unique interaction is initiated by the negatively charged bacterial cell walls, drawing the NPs towards them. TFG-mediated Co_3O_4 NPs, a vital component in this process, are postulated to disrupt the bacterial membrane structure, impairing permeability, interfering with crucial transport processes, and compromising the bacterial defense mechanisms. It has been reported that the antibacterial effectiveness of nanomaterials is closely affected by their physicochemical characteristics, such as their ability to generate reactive oxygen species (ROS), as well as their surface area, particle size, solubility, and surface charge.[112] For example, Co3O4 nanoparticles can accumulate in the outer membrane/cytoplasm. This accumulation may lead to the release of metal (cobalt) ions, which bind to biomolecules in the bacterial cell membrane through electrostatic interactions, causing depolarization and leading to cellular leakage.[113] For. Additionally, the excess production of ROS generated by these metal (cobalt) ions can penetrate the bacterial cell membrane and are capable of inducing substantial damage to critical cellular components such as DNA and proteins, ultimately resulting in bacterial cell death. In some instances, the NPs may breach the bacterial defenses, directly engaging with internal structures like mitochondria, leading to additional damage and cellular leakage. This intricate and multi-faceted assault is reflected in the substantial antibacterial activity observed against both *S. aureus* and *P. aeruginosa*. However, the efficacy of TFG-mediated Co_3O_4 NPs is not solely reliant on their intrinsic properties; rather, it is intricately linked to factors such as size, dosage, surface properties, TFG content, and treatment duration. Optimizing these parameters presents exciting prospects for further enhancing their antibacterial performance.

Beyond their inherent potency, the versatility of these NPs positions them as promising candidates for various applications. Their broad-spectrum effectiveness against both Gram-positive and Gram-negative bacteria makes them attractive for use in disinfectants and antimicrobial coatings, thereby safeguarding surfaces and materials from harmful microbial contamination. Moreover, in the context of escalating antibiotic resistance, TFG-mediated Co_3O_4 NPs emerge as a potential eco-friendly and effective alternative for bacterial control across diverse sectors, heralding a new era of antibacterial solutions with far-reaching implications. This innovative approach holds promise for addressing contemporary challenges in microbial control, opening avenues for sustainable and impactful antibacterial interventions.

The antimicrobial activity was assessed against two bacterial strains (Gram-positive *Staphylococcus aureus* and Gram-negative *Pseudomonas aeruginosa*). Although these are significant pathogens, the spectrum of antimicrobial activity should be further tested against a wider array of microbial species, including fungi and resistant bacterial strains, to fully understand the potential applications of these nanoparticles in diverse environments.

3.8.2. Comparison of antibacterial results with literature reports. The present study reveals a significantly enhanced antibacterial activity of Co_3O_4 synthesized using TFG compared to previously reported catalysts, as shown in Table 5. In this study, the catalyst exhibited an impressive ZOI against *S. aureus* (ZOI: 11.8 mm, 23.2 mm, and 26.6 mm at concentrations of 10 μg mL^{-1}, 25 μg mL^{-1}, and 40 μg mL^{-1}, respectively). This represents a substantial increase in antibacterial efficacy compared to other Co_3O_4 catalysts synthesized using different methods. For example, Co_3O_4 prepared with *Curcuma longa* achieved a maximum ZOI of 14 mm at 100 μg mL^{-1},[49] while the same catalyst synthesized with *Psidium guajava* showed a ZOI of 18 mm at 200 μg mL^{-1}.[102] In comparison to other antibacterial agents, such as Ag NPs synthesized using *Solanum melongena*, which achieved a ZOI of 15 mm against *S. aureus* at a concentration of 20 μg mL^{-1},[114] the present study demonstrates a comparable or superior antibacterial effect at a lower

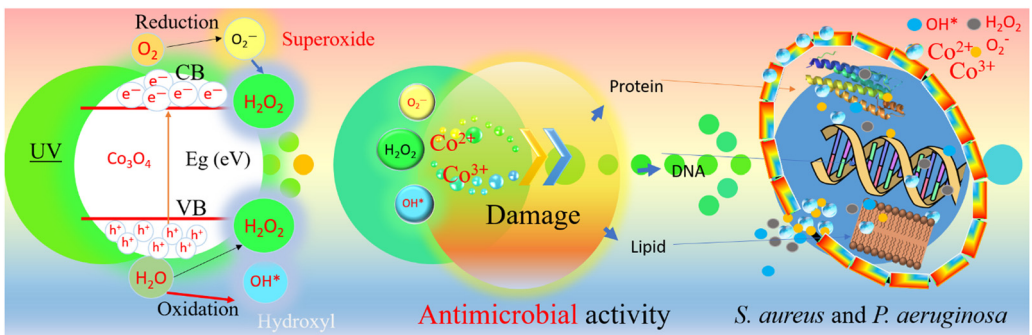

Fig. 13 Antimicrobial action mechanism of TFG-mediated Co_3O_4 NPs.

Table 5 Comparison of present antibacterial results with previous reports

S. no.	Catalyst	Method/Plant	Bacteria	Concentration (μg mL^{-1})	Approx. ZOI (mm)	Ref.
1	Co_3O_4	*Curcuma longa*	*S. aureus*	10	3	49
				20	5	
				50	8	
				100	14	
2	Co_3O_4	*Psidium guajava*	*S. aureus*	50	9	102
				100	12	
				150	16	
				200	18	
3	Co_3O_4	Chemical	*S. aureus*	500	21.17	116
4	ZnO	*Aspergillus niger*	*S. aureus*	—	10	117
5	Ag NPs	*Solanum melongena*	*S. aureus*	20	15	114
6	Ag	*Actinobacteria*	*S. aureus*	100	8	118
			P. aeruginosa	100	100	
7	ZnO	*Passiflora caerulea*	*P. aeruginosa*	50	10	115
8	ZnO	*Trigonella foenum-graecum*	*S. aureus*	50×10^3	10.3	113
				150×10^3	11.7	
			P. aeruginosa	50×10^3	14.3	
				150×10^3	17.0	
9	Co_3O_4	*Trigonella foenum-graecum*	*S. aureus*	10	11.8	Present work
				25	23.2	
				40	26.6	
			P. aeruginosa	10	8.0	
				25	13.4	
				40	19.6	

concentration of 25 μg mL^{-1}. Additionally, for *P. aeruginosa*, the present Co_3O_4 catalyst also showed enhanced activity with ZOI measurements of 8.0 mm, 13.4 mm, and 19.6 mm at concentrations of 10 μg mL^{-1}, 25 μg mL^{-1}, and 40 μg mL^{-1}, respectively. This is considerably higher than the ZOI achieved by ZnO synthesized using *Passiflora caerulea*, which recorded a ZOI of only 10 mm at 50 μg mL^{-1}.[115] Overall, the antibacterial performance of the present Co_3O_4 catalyst against both *S. aureus* and *P. aeruginosa* surpasses those of previously reported catalysts at comparable or even lower concentrations, underscoring its potential as a highly effective antimicrobial agent.

4. Conclusion

This study presents a novel and efficient method for synthesizing Co_3O_4 nanoparticles using TFG seed extract as a dual-functional agent. The TFG phytochemicals play a crucial role in stabilizing and directing the nanoparticle synthesis, resulting in well-defined morphologies and enhanced photocatalytic and antimicrobial properties. The synthesized Co_3O_4 NPs demonstrated exceptional photocatalytic efficiency, achieving 100% degradation of Congo Red dye within 60 minutes under UV irradiation, and showed strong antibacterial activity against both Gram-positive and Gram-negative bacteria. These findings highlight the potential of TFG-mediated Co_3O_4 nanoparticles in environmental remediation, particularly for wastewater treatment and combating antibiotic-resistant bacteria. Future research should focus on expanding the scope of photocatalytic testing under varying environmental conditions, exploring the antimicrobial activity against a broader range of microbial species, and assessing the scalability of the synthesis method for industrial applications.

Data availability

The data is available upon request.

Conflicts of interest

The authors asserted that they have no known financial or interpersonal conflicts that might have influenced the research provided in this paper.

Acknowledgements

The authors, Dr Sanjeev Kumar, Dr Supreet, and Dr Gautam Singh, would like to thank supporting Project No. (SUR/2020/004020), Science & Engineering Research Board (SERB), Govt. of India, for the financial support.

References

1 P. K. Dikshit, *et al.*, Green Synthesis of Metallic Nanoparticles: Applications and Limitations, *Catalysts*, 2021, **11**(8), 902.
2 A. K. Shimi, *et al.*, Green synthesis of SrO nanoparticles using leaf extract of Albizia julibrissin and its recyclable photocatalytic activity: An eco-friendly approach for treatment of industrial wastewater, *Environ. Sci.: Adv.*, 2022, **1**, 849–861.
3 G. Yashni, *et al.*, Bio-inspired ZnO NPs synthesized from Citrus sinensis peels extract for Congo red removal from textile wastewater via photocatalysis: Optimization, mechanisms, techno-economic analysis, *Chemosphere*, 2021, **281**, 130661.

4 A. Waris, *et al.*, Green fabrication of Co and Co(3)O(4) nanoparticles and their biomedical applications: A review, *Open Life Sci.*, 2021, **16**(1), 14–30.
5 A. Nyabadza, *et al.*, A review of physical, chemical and biological synthesis methods of bimetallic nanoparticles and applications in sensing, water treatment, biomedicine, catalysis and hydrogen storage, *Adv. Colloid Interface Sci.*, 2023, **321**, 103010.
6 S. Kumari, *et al.*, A comprehensive study on photocatalysis: materials and applications, *CrystEngComm*, 2024, **26**, 4886.
7 S. Ying, *et al.*, Green synthesis of nanoparticles: Current developments and limitations, *Environ. Technol. Innovation*, 2022, **26**, 102336.
8 M. Cowan Marjorie, Plant Products as Antimicrobial Agents, *Clin. Microbiol. Rev.*, 1999, **12**(4), 564–582.
9 P. Ansari, *et al.*, Protective Effects of Medicinal Plant-Based Foods against Diabetes: A Review on Pharmacology, Phytochemistry, and Molecular Mechanisms, *Nutrients*, 2023, **15**, 3266.
10 C. D. Nunes, *et al.*, Plants as Sources of Anti-Inflammatory Agents, *Molecules*, 2020, **25**, 3726.
11 G. Marslin, *et al.*, Secondary Metabolites in the Green Synthesis of Metallic Nanoparticles, *Materials*, 2018, **11**, 940.
12 C. L. Ventola, The antibiotic resistance crisis: part 1: causes and threats, *P T.*, 2015, **40**(4), 277.
13 B. Aslam, *et al.*, Antibiotic resistance: a rundown of a global crisis, *Infect. Drug Resist.*, 2018, **11**, 1645–1658.
14 P. V. Baptista, *et al.*, Nano-strategies to fight multidrug resistant bacteria—''A Battle of the Titans'', *Front. Microbiol.*, 2018, **9**, 1441.
15 Sachin, *et al.*, Green synthesis of zinc oxide nanoparticles using lychee peel and its application in anti-bacterial properties and CR dye removal from wastewater, *Chemosphere*, 2023, **327**, 138497.
16 S. R. E. Almisbah, *et al.*, Green synthesis of CuO nanoparticles using Hibiscus sabdariffa L. extract to treat wastewater in Soba Sewage Treatment Plant, Sudan, *Water Sci. Technol.*, 2023, **87**(12), 3059–3071.
17 W. M. Alamier, *et al.*, Green Synthesis of Silver Nanoparticles Using Acacia ehrenbergiana Plant Cortex Extract for Efficient Removal of Rhodamine B Cationic Dye from Wastewater and the Evaluation of Antimicrobial Activity, *ACS Omega*, 2023, **8**(21), 18901–18914.
18 C. P. Devatha, A. K. Thalla and S. Y. Katte, Green synthesis of iron nanoparticles using different leaf extracts for treatment of domestic waste water, *J. Cleaner Prod.*, 2016, **139**, 1425–1435.
19 N. K. Sethy, *et al.*, Green synthesis of TiO_2 nanoparticles from Syzygium cumini extract for photo-catalytic removal of lead (Pb) in explosive industrial wastewater, *Green Process. Synth.*, 2020, **9**(1), 171–181.
20 A. Fouda, *et al.*, Green Synthesis of Gold Nanoparticles by Aqueous Extract of Zingiber officinale: Characterization and Insight into Antimicrobial, Antioxidant, and In Vitro Cytotoxic Activities, *Appl. Sci.*, 2022, **12**, 12879.
21 L. S. Sundar, *et al.*, The cobalt oxide-based composite nanomaterial synthesis and its biomedical and engineering applications, *Cobalt Compounds and Applications*, IntechOpen, 2019.
22 M. Shinde, *et al.*, Synthesis of cobalt oxide nanostructures by microwave assisted solvothermal technique using binary solvent system, *Phys. Chem.*, 2015, **2**, 1.
23 A. Waris, *et al.*, Green fabrication of Co and Co_3O_4 nanoparticles and their biomedical applications: A review, *Open Life Sci.*, 2021, **16**(1), 14–30.
24 T. Warang, *et al.*, Co_3O_4 nanoparticles assembled coatings synthesized by different techniques for photo-degradation of methylene blue dye, *Appl. Catal., B*, 2013, **132–133**, 204–211.
25 G. Asha, *et al.*, Eco-friendly synthesis and characterization of cobalt oxide nanoparticles by sativum species and its photocatalytic activity, *Mater. Today: Proc.*, 2022, **48**, 486–493.
26 S. Dubey, *et al.*, Facile and green synthesis of highly dispersed cobalt oxide (Co_3O_4) nano powder: Characterization and screening of its eco-toxicity, *Adv. Powder Technol.*, 2018, **29**(11), 2583–2590.
27 A. T. Khalil, *et al.*, Physical properties, biological applications and biocompatibility studies on biosynthesized single phase cobalt oxide (Co3O4) nanoparticles via Sageretia thea (Osbeck.), *Arabian J. Chem.*, 2020, **13**(1), 606–619.
28 N. Matinise, *et al.*, Green synthesis of cobalt (II, III) oxide nanoparticles using Moringa Oleifera natural extract as high electrochemical electrode for supercapacitors, *AIP Conf. Proc.*, 2018, **1962**, 040005.
29 G. Marslin, *et al.*, Secondary Metabolites in the Green Synthesis of Metallic Nanoparticles, *Materials*, 2018, **11**, 940.
30 A. Diallo, *et al.*, Green synthesis of Co3O4 nanoparticles via Aspalathus linearis: Physical properties, *Green Chem. Lett. Rev.*, 2015, **8**(3–4), 30–36.
31 I. Bibi, *et al.*, Green and eco-friendly synthesis of cobalt-oxide nanoparticle: Characterization and photo-catalytic activity, *Adv. Powder Technol.*, 2017, **28**(9), 2035–2043.
32 A. Ahmad, *et al.*, Fenugreek a multipurpose crop: Potentialities and improvements, *Saudi J. Biol. Sci.*, 2016, **23**(2), 300–310.
33 N. Kadian, *et al.*, Structural and optical properties of gadolinium doped-magnetite nano-crystal for photocatalytic application, *J. Alloys Compd.*, 2023, **960**, 170811.
34 N. A. S. A. Hasona, *et al.*, Ameliorative properties of Iranian *Trigonella foenum-graecum* L. seeds and Punica granatum L. peel extracts in streptozotocin-induced experimental diabetic guinea pigs, *Asian Pac. J. Trop. Biomed.*, 2017, **7**(3), 234–239.
35 N. Methaq, M. Mahmood and I. Yahya, Nutrient and Phytochemical of Fenugreek (Trigonella Foenum graecum) Seeds, *Int. J. Sci.: Basic Appl. Res.*, 2017, **36**(3), 203–213.
36 S. Rohilla, *et al.*, Excellent UV-Light Triggered Photocatalytic Performance of ZnO.SiO_2 Nanocomposite for Water Pollutant Compound Methyl Orange Dye, *Nanomaterials*, 2021, **11**, 2548.

37 K. C. Nagulapalli Venkata, *et al.*, A small plant with big benefits: Fenugreek (*Trigonella foenum-graecum* Linn.) for disease prevention and health promotion, *Mol. Nutr. Food Res.*, 2017, **61**, 1600950.
38 N. Akhlaghi, G. Najafpour-Darzi and H. Younesi, Facile and green synthesis of cobalt oxide nanoparticles using ethanolic extract of Trigonella foenumgraceum (Fenugreek) leaves, *Adv. Powder Technol.*, 2020, **31**(8), 3562–3569.
39 H. Rizwana, *et al.*, Green synthesis, characterization, and antimicrobial activity of silver nanoparticles prepared using *Trigonella foenum-graecum* L. leaves grown in Saudi Arabia, *Green Process. Synth.*, 2021, **10**(1), 421–429.
40 M. Moond, *et al.*, Biosynthesis of Silver Nanoparticles Utilizing Leaf Extract of *Trigonella foenum-graecum* L. for Catalytic Dyes Degradation and Colorimetric Sensing of Fe^{3+}/Hg^{2}, *Molecules*, 2023, **28**, 951.
41 M. kermani, *et al.*, The photocatalytic, cytotoxicity, and antibacterial properties of zinc oxide nanoparticles synthesized using *Trigonella foenum-graecum* L extract, *Environ. Sci. Pollut. Res.*, 2023, **30**(7), 19313–19325.
42 S. Subhapriya and P. Gomathipriya, Green synthesis of titanium dioxide (TiO_2) nanoparticles by *Trigonella foenum-graecum* extract and its antimicrobial properties, *Microb. Pathog.*, 2018, **116**, 215–220.
43 H. Kaur, S. Kumar and G. Bouzid, Exploring the role of different phytochemicals on the morphological variations of metal and metal oxide nanomaterials for biomedical application, *Interactions*, 2024, **245**(1), 234.
44 N. Akhlaghi, G. Najafpour-Darzi and H. J. A. P. T. Younesi, Facile and green synthesis of cobalt oxide nanoparticles using ethanolic extract of Trigonella foenumgraceum (Fenugreek) leaves, *Adv. Powder Technol.*, 2020, **31**, 3562–3569.
45 C. Anuradha and P. J. M. R. E. Raji, Effect of annealing temperature on antibacterial, antifungal and structural properties of bio-synthesized Co_3O_4 nanoparticles using Hibiscus Rosa-sinensis, *Mater. Res. Express*, 2019, **6**(9), 095063.
46 L. Han, D. P. Yang and A. Liu, Leaf-templated synthesis of 3D hierarchical porous cobalt oxide nanostructure as direct electrochemical biosensing interface with enhanced electrocatalysis, *Biosens. Bioelectron.*, 2015, **63**, 145–152.
47 A. I. Khadhim and R. E. Kadhim, Synthesis of Cobalt Nanoparticles Biologically by Conocarpus erectus L. Aqueous Leaves Extract, *Ann. Romanian Soc. Cell Biol.*, 2021, 5361–5372.
48 S. Kumar, *et al.*, Potential of Piper betle@Co_3O_4 nanoparticles as high-performance photocatalysts for the removal of industrial dyes, *J. Cleaner Prod.*, 2022, **361**, 132242.
49 P. Chelliah, *et al.*, Green Synthesis and Characterizations of Cobalt Oxide Nanoparticles and Their Coherent Photocatalytic and Antibacterial Investigations, *Water*, 2023, **15**, 910.
50 S. Haq, *et al.*, Green synthesis of cobalt oxide nanoparticles and the effect of annealing temperature on their physiochemical and biological properties, *Mater. Res. Express*, 2021, **8**(7), 075009.
51 P. Gowthami, *et al.*, Biosynthesis of Co_3O_4 nanomedicine by using Mollugo oppositifolia L. aqueous leaf extract and its antimicrobial, mosquito larvicidal activities, *Sci. Rep.*, 2023, **13**(1), 9002.
52 M. K. Uddin and U. Baig, Synthesis of Co_3O_4 nanoparticles and their performance towards methyl orange dye removal: Characterisation, adsorption and response surface methodology, *J. Cleaner Prod.*, 2019, **211**, 1141–1153.
53 B. Senthil, *et al.*, Non-cytotoxic effect of green synthesized silver nanoparticles and its antibacterial activity, *J. Photochem. Photobiol., B*, 2017, **177**, 1–7.
54 S. Farhadi, M. Javanmard and G. Nadri, Characterization of Cobalt Oxide Nanoparticles Prepared by the Thermal Decomposition of $[Co(NH_3)_5(H_2O)](NO_3)_3$ Complex and Study of Their Photocatalytic Activity, *Acta Chim. Slovaca*, 2016, **63**(2), 335.
55 M. Naseri, *et al.*, Structure and Physical Properties of NiO/Co_3O_4 Nanoparticles, *Metals*, 2016, **6**, 181.
56 Y. Zheng, *et al.*, Controllable growth of cobalt oxide nanoparticles on reduced graphene oxide and its application for highly sensitive glucose sensor, *Int. J. Electrochem. Sci.*, 2014, **9**, 7369–7381.
57 B. A. Al Jahdaly, *et al.*, Phytosynthesis of Co_3O_4 Nanoparticles as the High Energy Storage Material of an Activated Carbon/Co_3O_4 Symmetric Supercapacitor Device with Excellent Cyclic Stability Based on a Na_2SO_4 Aqueous Electrolyte, *ACS Omega*, 2022, **7**, 23673.
58 A. Kumar, *et al.*, In situ decoration of silver nanoparticles on single-walled carbon nanotubes by microwave irradiation for enhanced and durable anti-bacterial finishing on cotton fabric, *Ceram. Int.*, 2019, **45**, 1011–1019.
59 M. Yarestani, *et al.*, Hydrothermal synthesis of cobalt oxide nanoparticles: Its optical and magnetic properties, *J. Sci.*, 2014, **25**(4), 339–343.
60 Q. Y. Chen, *et al.*, Temperature effect on green-synthesized Co_3O_4 nanoparticle as photocatalyst for overall water splitting, *J. Photonics Energy*, 2020, **10**(4), 042006.
61 S. A. David, *et al.*, Synthesis and characterization of Cobalt Oxide nanoparticles using Momordica charantia and its photocatalytic activity, *Int. J. Nano Dimens.*, 2022, **13**(3), 335–343.
62 C. Anuradha and P. Raji, Facile synthesis and characterization of Co_3O_4 nanoparticles for high-performance supercapacitors using Camellia sinensis, *Appl. Phys. A: Mater. Sci. Process.*, 2020, **126**, 1–12.
63 J. K. Sharma, *et al.*, Green synthesis of Co_3O_4 nanoparticles and their applications in thermal decomposition of ammonium perchlorate and dye-sensitized solar cells, *Mater. Sci. Eng., B*, 2015, **193**, 181–188.
64 K. Kombaiah, *et al.*, Green Synthesis of Co_3O_4 Nanorods for Highly Efficient Catalytic, Photocatalytic, and Antibacterial Activities, *J. Nanosci. Nanotechnol.*, 2019, **19**(5), 2590–2598.
65 C. M. Magdalane, *et al.*, Structural and morphological properties of Co_3O_4 nanostructures: Investigation of low temperature oxidation for photocatalytic application for waste water treatment, *Surf. Interfaces*, 2019, **17**, 100369.

66 F. K. Sabir, *et al.*, Synthesis of Cobalt Oxide Nanoparticles Through Chemical and Biological Pathways for Antibacterial Activity, *J. Nanostruct.*, 2021, **11**(3), 577–587.
67 R. V. Poonguzhali, *et al.*, Natural lemon extract assisted green synthesis of spinel Co3O4 nanoparticles for LPG gas sensor application, *Sens. Actuators, B*, 2023, **377**, 133036.
68 V. Nagal, *et al.*, Highly Sensitive Electrochemical Non-Enzymatic Uric Acid Sensor Based on Cobalt Oxide Puffy Balls-Like Nanostructure, *Biosensors*, 2023, **13**, 375.
69 G. Marimuthu, *et al.*, Nanorod like $NiCo_2O_4$ nanostructure for high sensitive and selective ammonia gas sensor, *J. Mater. Sci.: Mater. Electron.*, 2020, 31.
70 T. H. Vu, P. T. Nguyen and M. Kim, Polydopamine-Coated Co_3O_4 Nanoparticles as an Efficient Catalase Mimic for Fluorescent Detection of Sulfide Ion, *Biosensors*, 2022, **12**, 1047.
71 Q. Y. Chen, *et al.*, Temperature effect on green-synthesized Co_3O_4 nanoparticle as photocatalyst for overall water splitting, *J. Photonics Energy*, 2020, **10**, 042006.
72 A. Zuhrotun, D. J. Oktaviani and A. N. Hasanah, Biosynthesis of Gold and Silver Nanoparticles Using Phytochemical Compounds, *Molecules*, 2023, **28**, 3240.
73 K. A. Hamed, *et al.*, Assessing the Efficacy of Fenugreek Saponin Nanoparticles in Attenuating Nicotine-Induced Hepatotoxicity in Male Rats, *ACS Omega*, 2023, **8**(45), 42722–42731.
74 K. Bhardwaj, *et al.*, Biogenic Metallic Nanoparticles from Seed Extracts: Characteristics, Properties, and Applications, *J. Nanomater.*, 2022, 2271278.
75 A. B. Hirpara, *et al.*, Biological investigation of sonochemically synthesized CZTS nanoparticles, *Appl. Surf. Sci. Adv.*, 2022, **12**, 100338.
76 S. Mourdikoudis, R. M. Pallares and N. T. J. N. Thanh, Characterization techniques for nanoparticles: comparison and complementarity upon studying nanoparticle properties, *Nanoscale*, 2018, **10**(27), 12871–12934.
77 L. Belles, *et al.*, Flame Spray Pyrolysis Co_3O_4/CoO as Highly-Efficient Nanocatalyst for Oxygen Reduction Reaction, *Nanomaterials*, 2021, 11, DOI: **10.3390/nano11040925**.
78 S. Luo, *et al.*, Nanoscale Parallel Circuitry Based on Interpenetrating Conductive Assembly for Flexible and High-Power Zinc Ion Battery, *Adv. Funct. Mater.*, 2019, **29**(28), 1901336.
79 J. Jeevanandam, *et al.*, Review on nanoparticles and nanostructured materials: history, sources, toxicity and regulations, *Beilstein J. Nanotechnol.*, 2018, **9**, 1050–1074.
80 B. Serment, *et al.*, The versatile Co^{2+}/Co^{3+} oxidation states in cobalt alumina spinel: how to design strong blue nanometric pigments for color electrophoretic display, *RSC Adv.*, 2019, **9**(59), 34125–34135.
81 S. Y. Zhang, *et al.*, Co_3O_4 polyhedrons with enhanced electric conductivity as efficient water oxidation electrocatalysts in alkaline medium, *J. Mater. Sci.*, 2018, 53.
82 S. Porcu, F. Secci and P. C. Ricci, Advances in Hybrid Composites for Photocatalytic Applications: A Review, *Molecules*, 2022, **27**, 6828.
83 A. K. Singh, A review on plant extract-based route for synthesis of cobalt nanoparticles: Photocatalytic, electrochemical sensing and antibacterial applications, *Curr. Res. Green Sustainable Chem.*, 2022, **5**, 100270.
84 Z. Wu, *et al.*, Facile synthesis and excellent electrochemical performance of reduced graphene oxide-Co_3O_4 yolk-shell nanocage as a catalyst for oxygen evolution reaction, *J. Mater. Chem. A*, 2016, 4.
85 N. Akhlaghi, G. Najafpour and H. Younesi, Facile and green synthesis of cobalt oxide nanoparticles using ethanolic extract of Trigonella foenumgraceum (Fenugreek) leaves, *Adv. Powder Technol.*, 2020, 31.
86 M. E. Malefane, Co(3)O(4)/Bi(4)O(5)I(2)/Bi(5)O(7)I C-Scheme Heterojunction for Degradation of Organic Pollutants by Light-Emitting Diode Irradiation, *ACS Omega*, 2020, **5**(41), 26829–26844.
87 C. Y. Toe, *et al.*, Advancing photoreforming of organics: highlights on photocatalyst and system designs for selective oxidation reactions, *Energy Environ. Sci.*, 2021, **14**(3), 1140–1175.
88 H. Dai, *et al.*, Confinement boosted heterogeneous advanced oxidation processes, *Chem. Eng. J.*, 2023, **472**, 144861.
89 Y. L. Pang, *et al.*, Enhancement of photocatalytic degradation of organic dyes using ZnO decorated on reduced graphene oxide (rGO), *Desalin. Water Treat.*, 2018, **108**, 311–321.
90 M. Aminuzzaman, *et al.*, Value-adding to dragon fruit (Hylocereus polyrhizus) peel biowaste: green synthesis of ZnO nanoparticles and their characterization, *Inorg. Nano-Met. Chem.*, 2019, **49**(11), 401–411.
91 T. Muhmood, *et al.*, Graphene-like graphitic carbon nitride (g-C_3N_4) as a semiconductor photocatalyst: Properties, classification, and defects engineering approaches, *Mater. Today Sustainability*, 2024, **25**, 100633.
92 T. H. Lai, K. I. Katsumata and Y. J. Hsu, In situ charge carrier dynamics of semiconductor nanostructures for advanced photoelectrochemical and photocatalytic applications, *Nanophotonics*, 2021, **10**(2), 777–795.
93 A. Baez and J. Shiloach, Escherichia coli avoids high dissolved oxygen stress by activation of SoxRS and manganese-superoxide dismutase, *Microb. Cell Fact.*, 2013, **12**(1), 23.
94 M. Long, *et al.*, Efficient Photocatalytic Degradation of Phenol over Co_3O_4/$BiVO_4$ Composite under Visible Light Irradiation, *J. Phys. Chem. B*, 2006, **110**, 20211.
95 S. G. Kumar and K. Rao, Zinc oxide based photocatalysis: tailoring surface-bulk structure and related interfacial charge carrier dynamics for better environmental applications, *RSC Adv.*, 2015, **5**(5), 3306–3351.
96 M. R. Martinez and K. J. C. C. Matyjaszewski, Degradable and recyclable polymers by reversible deactivation radical polymerization, *CCS Chem.*, 2022, **4**(7), 2176–2211.
97 C. Sidney Santana, *et al.*, Kinetic Evaluation of Dye Decolorization by Fenton Processes in the Presence of 3-Hydroxyanthranilic Acid, *Int. J. Environ. Res. Public Health*, 2019, **16**, 1602.
98 M. S. Samuel, *et al.*, Green synthesis of cobalt-oxide nanoparticle using jumbo Muscadine (Vitis rotundifolia):

Characterization and photo-catalytic activity of acid Blue-74, *J. Photochem. Photobiol., B*, 2020, **211**, 112011.

99 M. Verma, *et al.*, Efficient photocatalytic degradation of Malachite green dye using facilely synthesized cobalt oxide nanomaterials using citric acid and oleic acid, *J. Phys. Chem. Solids*, 2021, **155**, 110125.

100 M. Aminuzzaman, *et al.*, Green synthesis of zinc oxide nanoparticles using aqueous extract of Garcinia mangostana fruit pericarp and their photocatalytic activity, *Bull. Mater. Sci.*, 2018, **41**(2), 50.

101 H. Kaur, *et al.*, An emerging expanse: Novel and eco-friendly-biogenic synthesis of E. cardamomum-wrapped TiO_2 nanoparticles for environmental and biological applications, *Environ. Res.*, 2023, **234**, 116599.

102 R. Govindasamy, *et al.*, Green Synthesis and Characterization of Cobalt Oxide Nanoparticles Using Psidium guajava Leaves Extracts and Their Photocatalytic and Biological Activities, *Molecules*, 2022, **27**, 5646, DOI: **10.3390/molecules27175646**.

103 R. Shanmuganathan, *et al.*, Green synthesized Cobalt oxide nanoparticles using Curcuma longa for anti-oxidant, anti-microbial, dye degradation and anti-cancer property, *Environ. Res.*, 2023, **236**, 116747.

104 T. B. Mbuyazi and P. A. Ajibade, Photocatalytic Degradation of Organic Dyes by Magnetite Nanoparticles Prepared by Co-Precipitation, *Int. J. Mol. Sci.*, 2024, **25**, 7876.

105 M. Gurusamy, M. Sellavel and V. Kuppuvelsamy, A sustainable green synthesis for photocatalytic and antibacterial activity of zinc oxide nanoparticles using Cucumis maderaspatanus leaf extract, *Desalin. Water Treat.*, 2024, **319**, 100457.

106 S. A. Mousa, *et al.*, Enhanced photocatalytic activity of green synthesized zinc oxide nanoparticles using low-cost plant extracts, *Sci. Rep.*, 2024, **14**(1), 16713.

107 H. Kaur, *et al.*, One-pot biogenic synthesis of C. limon/TiO_2 with dual applications as an advance photocatalyst and antimicrobial agent, *Chemosphere*, 2023, **335**, 139106.

108 M. Aminuzzaman, L. M. Kei and W. H. Liang, Green synthesis of copper oxide (CuO) nanoparticles using banana peel extract and their photocatalytic activities, *AIP Conf. Proc.*, 2017, **1828**(1), 020016.

109 D. B. Manikandan, *et al.*, Biofabrication of ecofriendly copper oxide nanoparticles using Ocimum americanum aqueous leaf extract: analysis of in vitro antibacterial, anticancer, and photocatalytic activities, *Environ. Sci. Pollut. Res.*, 2021, **28**(26), 33927–33941.

110 R. Katwal, *et al.*, Electrochemical synthesized copper oxide nanoparticles for enhanced photocatalytic and antimicrobial activity, *J. Ind. Eng. Chem.*, 2015, **31**, 173–184.

111 S. Aroob, *et al.*, Green Synthesis and Photocatalytic Dye Degradation Activity of CuO Nanoparticles, *Catalysts*, 2023, **13**, 502.

112 Y. B. Chan, *et al.*, Green synthesis of ZnO nanoparticles using the mangosteen (Garcinia mangostana L.) leaf extract: Comparative preliminary in vitro antibacterial study, *Green Process. Synth.*, 2024, **13**, 20230251.

113 V. Selvanathan, *et al.*, Synthesis, characterization, and preliminary in vitro antibacterial evaluation of ZnO nanoparticles derived from soursop (Annona muricata L.) leaf extract as a green reducing agent, *J. Mater. Res. Technol.*, 2022, **20**, 2931–2941.

114 K. Pushparaj, *et al.*, Green synthesis, characterization of silver nanoparticles using aqueous leaf extracts of Solanum melongena and in vitro evaluation of antibacterial, pesticidal and anticancer activity in human MDA-MB-231 breast cancer cell lines, *J. King Saud Univ., Sci.*, 2023, **35**(5), 102663.

115 J. Santhoshkumar, S. V. Kumar and S. Rajeshkumar, Synthesis of zinc oxide nanoparticles using plant leaf extract against urinary tract infection pathogen, *Resour.-Effic. Technol.*, 2017, **3**(4), 459–465.

116 V. Gupta, *et al.*, Comparative evaluation of antibacterial potentials of nano cobalt oxide with standard antimicrobials, *J. Indian Chem. Soc.*, 2022, **99**(7), 100533.

117 V. N. Kalpana, *et al.*, Biosynthesis of zinc oxide nanoparticles using culture filtrates of Aspergillus niger: Antimicrobial textiles and dye degradation studies, *OpenNano*, 2018, **3**, 48–55.

118 V. Railean-Plugaru, *et al.*, Antimicrobial properties of biosynthesized silver nanoparticles studied by flow cytometry and related techniques, *Electrophoresis*, 2016, **37**(5–6), 752–761.